



저작자표시-비영리-변경금지 2.0 대한민국

이용자는 아래의 조건을 따르는 경우에 한하여 자유롭게

- 이 저작물을 복제, 배포, 전송, 전시, 공연 및 방송할 수 있습니다.

다음과 같은 조건을 따라야 합니다:



저작자표시. 귀하는 원저작자를 표시하여야 합니다.



비영리. 귀하는 이 저작물을 영리 목적으로 이용할 수 없습니다.



변경금지. 귀하는 이 저작물을 개작, 변형 또는 가공할 수 없습니다.

- 귀하는, 이 저작물의 재이용이나 배포의 경우, 이 저작물에 적용된 이용허락조건을 명확하게 나타내어야 합니다.
- 저작권자로부터 별도의 허가를 받으면 이러한 조건들은 적용되지 않습니다.

저작권법에 따른 이용자의 권리는 위의 내용에 의하여 영향을 받지 않습니다.

이것은 [이용허락규약\(Legal Code\)](#)을 이해하기 쉽게 요약한 것입니다.

[Disclaimer](#)

Doctoral Thesis

# Development of Quasi-Optical Millimeter- and THz-wave System for Probing Plasma Density

Mun Seok Choe

Department of Physics

Graduate School of UNIST

2019

# Development of Quasi-Optical Millimeter- and THz-wave System for Probing Plasma Density

Mun Seok Choe

Department of Physics

Graduate School of UNIST

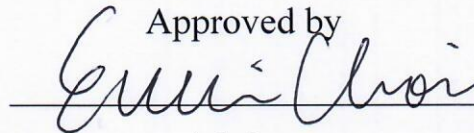
# Development of Quasi-Optical Millimeter- and THz-wave System for Probing Plasma Density

A thesis/dissertation  
submitted to the Graduate School of UNIST  
in partial fulfillment of the  
requirements for the degree of  
Doctor of Philosophy

Mun Seok Choe

06/05/2019 of submission

Approved by



Advisor

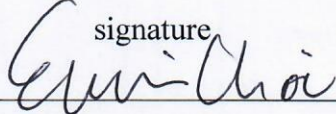
EunMi Choi

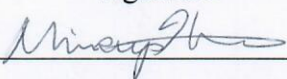
# Development of Quasi-Optical Millimeter- and THz-wave System for Probing Plasma Density

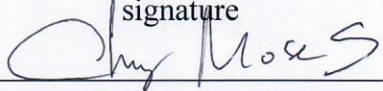
Mun Seok Choe

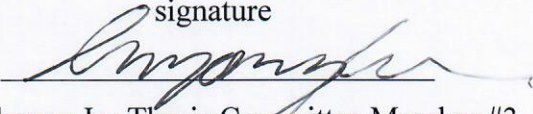
This certifies that the thesis/dissertation of Mun Seok Choe is approved.

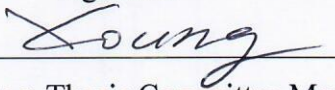
06/05/2019 of submission

signature  
  
Advisor: EunMi Choi

signature  
  
Min Sup Hur: Thesis Committee Member #1

signature  
  
Moses Chung: Thesis Committee Member #2

signature  
  
Yongkyoon In: Thesis Committee Member #3

signature  
  
Young Soon Bae: Thesis Committee Member #4;

## Abstract

Quasi-optical millimeter- and terahertz (THz)-wave technique in free-space is widely used to measure material characteristics such as a high-k dielectric material, a semi-conductor, plasma and biomolecules. As THz based science and technology have been developed, the low-loss transmission system also has become important in millimeter- and THz-wave applications because development of high-power sources and detector have limitations. Therefore, millimeter- and THz-wave is easily attenuated in air.

This thesis presents fundamental concepts of quasi-optical millimeter- and THz-wave probing system to diagnose charge carrier density of semi-conductor and plasma density. As a semi-conductor application, we present the experimental results of the measuring carrier lifetime of semi-conductor using proposed quasi-optical photo-conductivity decay method (QO-PCD). The developed QO-PCD system consist of optical pumping laser (Nd:YAG laser, 532 nm, 15~18 ns,  $0.27 \pm 0.02$  W at 100 Hz repetition), a 95 GHz source consisting of vector network analyzer (VNA) with amplifier, a Schottky diode detector, the Gaussian horn antennas, the quasi-optical off-axis ellipsoidal mirrors and a semi-insulating silicon (Si) wafer for proof of concept study. As results, the initial excess carrier density was measured to be  $1.5 \times 10^{15} \text{ cm}^{-3}$  and the carrier lifetime was measured to be  $30.6 \mu\text{s}$  in Si wafer (460  $\mu\text{m}$  thickness,  $> 4000 \text{ ohm}\cdot\text{cm}$  resistivity). The 2D distribution of carrier lifetime was also measured using a motion controller with automatic algorithm.

In plasma part, we report that the experimental results of quasi-optical plasma diagnostics system with inductively coupled plasma (ICP) chamber for generating high-density plasma. In addition, we show that this ICP chamber can be applied to a plasma switching system for the study of high-power millimeter-wave in pulsed plasma. A helical type ICP chamber is designed for high transmission of Gaussian beam (linear polarized E-field having Gaussian profiled) and generation of high-density bulked plasma. The inductive rf discharged plasma can be generated in range of  $10^{13} \sim 10^{14} \text{ cm}^{-3}$  with a pressure range of a few Torr (2~5 Torr). In this condition, we can find plasma cut-off frequency using VNA as a source of millimeter-wave (F-band, 90~140 GHz). In frequency sweep, the millimeter-wave under plasma cut-off frequency cannot penetrate to plasma layer. These results are expressed by S21 parameter of VNA in frequency domain. Based on this experimental data, we can extract complex permittivity of plasma to estimate plasma density and effective collision frequency. Furthermore, axisymmetric two-dimensional multi-layered plasma model is proposed in high-pressure and high-density plasma conditions. This model is good agreement with measured data.

The developed ICP chamber was applied to fast control technique of high-power millimeter-wave using pulsed plasma. Using RF pulsing in RF generator (13.56 MHz, 1000 W), a pulsed plasma is generated with few kHz repetitions for fusion plasma applications. For proof-of-concept study, we

conducted cold test using VNA (low power millimeter-wave,  $<1\text{mW}$ , continuous waves (CW)) and successfully demonstrated proto-type test of millimeter-wave switching having 2 kHz repetition. For hot test, a gyrotron at UNIST (95 GHz, 20 kW of power) is used as a high-power millimeter-wave source. Although the gyrotron pulse length (20 us) is not enough to measure switching results (plasma switching time is 200 us), we observed wave absorption in plasma and increase of plasma density simultaneously. We show the possibility of fast control of high-power millimeter-wave and experimental study of plasma heating mechanism by high-power millimeter-wave.

In conclusion, these all results will contribute to development of THz transmission system in free space for THz material characterization applications. Furthermore, we believe that the proposed techniques will be standard in THz research area.





## Contents

Abstract.....	v
Contents .....	viii
List of Figures .....	x
List of Tables .....	xii
<b>Chapter 1</b> Introduction.....	1
1.1 Overview of millimeter- and THz-waves in free space and complex dielectric media .....	1
1.2 Thesis outline .....	2
<b>Chapter 2</b> Concept of quasi-optical transmission system in millimeter- and THz-waves.....	3
2.1 Low loss quasi-optical transmission system .....	3
2.1.1 Gaussian beam using corrugated horn antenna .....	3
2.1.2 Quasi-optical mirror with mode matching technique.....	5
2.1.3 Oversized corrugated waveguide for HE <sub>11</sub> mode transmission .....	8
2.2 Theory of complex permittivity measurement using quasi-optical technique .....	12
<b>Chapter 3</b> Measurement of the carrier lifetime in semi-conductor using a quasi-optical millimeter and THz waves .....	16
3.1 Concept of carrier lifetime measurement in semi-conductor .....	16
3.2 Quasi-optical photoconductivity decay (QO-PCD) method .....	20
3.2.1 Theory of photoconductivity decay .....	20
3.2.2 Experimental setup of quasi-optical system.....	21
3.3 Experimental study of QO-PCD system .....	27
<b>Chapter 4</b> Characteristics of high-power millimeter-wave in pulsed plasma.....	30
4.1 Motivation.....	30
4.2 Design of inductive rf discharged high-density plasma .....	31
4.3 Experimental setup of Plasma switching system .....	34
4.3.1 Experimental setup.....	34
4.3.2 Analysis of pulsed plasma using non-invasive millimeter-wave .....	37
4.3.3 Axisymmetric two-dimensional multi-layer model for plasma sheath .....	37
4.4 Fast control of high-power millimeter pulse in pulsed plasma .....	42
4.4.1 Gyrotron: high-power millimeter wave source .....	42
4.4.2 Focusing mirror.....	43
4.4.3 Experimental setup.....	46

4.4.4 Absorption of high-power millimeter wave in steady-state plasma.....	48
4.4.5 High-power millimeter-wave in pulsed plasma for plasma switching system.....	50
<b>Chapter 5 Conclusion .....</b>	<b>54</b>
References.....	56

## List of Figures

Figure 2-1. Geometry of quasi-optical ellipsoidal mirror .....	7
Figure 2-2. Geometry of quasi-optical parabolic mirror .....	7
Figure 2-3. Structure of corrugated waveguide .....	8
Figure 2-4. Electric field patterns of each TE and TM modes in hybrid modes .....	9
Figure 2-5. Higher order modes in HE mode.....	10
Figure 2-6. Higher order modes in EH mode.....	11
Figure 2-7. A photo-excited media between two dielectric media.....	12
Figure 2-8 Multi-layered complex media between dielectric media.....	14
Figure 3-1. Carrier lifetime in semi-conductor .....	17
Figure 3-2. Concept of measuring carrier lifetime using EM wave.....	18
Figure 3-3. Reflectance of EM wave in semi-conductor .....	18
Figure 3-4. EM probes in u-PCD technique .....	19
Figure 3-5. Beam size depending on frequency.....	19
Figure 3-6. The path of gaussian beam with and without photo-excitations in 2D simulation (COMSOL Multiphysics).....	21
Figure 3-7. Schematic of QO-PCD.....	22
Figure 3-8. Quasi-optical transmission simulation using Surf3D code .....	23
Figure 3-9 Surf3D results of Gaussian beam at sample position .....	23
Figure 3-10. Surf3D results of Gaussian beam at receiver position .....	24
Figure 3-11. Free space permittivity measurement using quasi-optical system.....	24
Figure 3-12. Experimental result of free space loss in quasi-optical system .....	25
Figure 3-13. Transmittance results of semi-insulating Si wafer in QO transmission systems.....	25
Figure 3-14. The experimental setup of QO-PCD .....	27
Figure 3-15. RF transmittance signal with optical pumping compared to the theoretical model. ....	28
Figure 3-16. (a) 2D mapping results of carrier lifetime, (b) calibration error graph.....	29
Figure 4-1. Helical structure of the ICP with designed parameters .....	31
Figure 4-2. Impedance measurement of ICP chamber (Frequency sweep: 0 ~ 20 MHz) .....	33
Figure 4-3. (a) Simulation results of QO-OAP mirrors using Surf3D code (b) Specifications of Gaussian beam in QO system. ....	35
Figure 4-4. (a) Free space transmission loss in QO systems (5% smoothing) (b) Transmittance of two quartz windows in plasma chamber .....	35
Figure 4-5. Schematic of ICP diagnosis using the quasi-optical millimeter-wave system: (a) ICP system; (b) quasi-optical millimeter-wave system; and (c) close-up of the experimental Ar ICP	

plasma (Pressure: 2 Torr, RF power: 1000 W) .....	36
Figure 4-6. Experimental results of transmittance (S21) by EM-field penetrated from plasma: (a) RF power variations at 2 Torr; (b) pressure variations at 700 W .....	36
Figure 4-7. S21 (transmittance) result of experimental data compared to the axisymmetric 2D multi-layered models (flat-top and Bessel) data fitting (Ar gas, RF power: 1,000 W, pressure: 2 Torr).....	39
Figure 4-8. (a) The comparison of plasma density distributions between radial plasma models (r-axis, flat-top and Bessel models) (b) The axial plasma density distribution (z-axis, cosine model) .....	39
Figure 4-9. Axisymmetric 2D multi-layered model with Gaussian-beam propagation .....	40
Figure 4-10. (a) Graph of plasma densities vs. RF power via the fitting model (Std. Dev.= $\pm 0.01 \times 10^{14} \text{ cm}^{-3}$ ). (b) Graph of effective collision frequencies vs. pressure via the fitting model (Std. Dev.= $\pm 4.18 \times 10^8 \text{ Hz}$ ).....	40
Figure 4-11. Estimated effective plasma-sheath thickness by theoretical modeling.....	41
Figure 4-12. UNIST W-band gyrotron.....	42
Figure 4-13. Focusing mirror for gaussian beam injection .....	43
Figure 4-14. CST MWS simulation of reflection gain measurement in focusing mirror .....	43
Figure 4-15. Focused gaussian beam at plasma chamber with designed focusing mirror mesh.....	44
Figure 4-16. The experimental setup of high-power millimeter-wave absorption in pulsed plasma Focused gaussian beam at plasma chamber with designed focusing mirror mesh.....	44
Figure 4-17. The experimental setup of high-power millimeter-wave absorption in pulsed plasma ....	46
Figure 4-18. Gyrotron alignment using field tracing on liquid crystal paper .....	47
Figure 4-19. Gyrotron beam 1D scan results at focusing mirror position.....	47
Figure 4-20. COMSOL Multiphysics simulation (a) Plasma density distribution (b) Gaussian beam absorption in plasma (Initial peak plasma density: $1.08 \times 10^{14} \text{ cm}^{-3}$ , Effective collision frequency: 5.15GHz).....	48
Figure 4-21. Transmittance, reflectance and absorption of Gaussian beam in plasma (COMSOL Multiphysics).....	49
Figure 4-22 (a) Transmittance of gyrotron pulse with RF power dependence (b) Reflectance of gyrotron pulse with RF power dependence (c) Photodetector signal with RF power dependence ....	49
Figure 4-23. Experimental setup of low-power millimeter-wave switching test.....	50
Figure 4-24. Experimental results of low-power millimeter-wave switching test.....	51
Figure 4-25. Comparison of lower-power test and high-power test .....	51
Figure 4-26. Selective injection of gyrotron pulse in pulsed plasma using pulse synchronization .....	52
Figure 4-27. Selective injections of Gaussian beam in pulsed plasma. ....	52
Figure 4-28. The transmittances of Gaussian beam in pulsed plasma at each selective injection. ....	53

## List of Tables

Table 1. Mixed field components in HE11 modes .....	9
Table 2. The specifications of 1 <sup>ST</sup> QO-OAE mirror .....	26
Table 3. The specifications of 2 <sup>nd</sup> QO-OAE mirror .....	26
Table 4. The experimental results of QO-PCD .....	28

## Abbreviations and Acronyms

$\mu\text{m}$	Micrometer
$\mu\text{-PCD}$	Microwave photoconductivity decay method
2D	Two-dimensional
Ar	Argon
CH	Channel
cm	Centimeter
CNC	Computer numerical control
CW	Continues wave
Db	Decibel
dBm	Decibel-milliwatts
ECCD	Electron cyclotron current drive
ECH & CD	Electron cyclotron heating and current drive
EM	Electromagnetic
FEM	Finite element method
FWHM	Full width at half maximum
GHz	Gigahertz
HE and EH	Hybrid modes
ICP	Inductively coupled plasma
kHz	Kilohertz
kW	Kilo-watt
MFC	Mass flow controller
MHz	Megahertz
mm	Millimeter
MOU	Matching optics unit
mW	Milli-watt
MWS	Microwave studio
Nd: YAG	Neodymium-doped yttrium aluminum garnet
NTMs	Neoclassical tearing modes
QO	Quasi-optical
QO-OAE	Quasi-optical off-axis ellipsoidal
QO-OAP	Quasi-optical off-axis parabolic
QO-PCD	Quasi-optical photoconductivity decay
RF	Radio-frequency
Si	Silicon
SNR	Signal-to-noise ratio

TE	Transverse electric
THz	Terahertz
THz-TDS	Terahertz time domain spectroscopy
TM	Transverse magnetic
UNIST	Ulsan National Institute of Science and Technology
us	Microseconds
V	Volts
VNA	Vector network analyzer
W	Watts

# Chapter 1

## Introduction

### 1.1 Overview of millimeter- and THz-waves in free space and complex dielectric media

The concept of electromagnetic (EM)-wave propagation in free space is widely used in all science and technology areas since EM wave is discovered. While microwave has been developed with electronics and infrared, light, X-ray have been developed with photonics, millimeter- and terahertz (THz)-wave (or submillimeter-wave) development has been delayed by “THz-gap”. As micro-fabricated and Nano-material technologies are rapidly developed since 1990s, various millimeter- and THz-wave sources and detectors have been developed from electronics and photonics at each section. Accordingly, many of researchers shows that THz technology can be applied to a lot of fields such as communication, security, radar, medical science and non-invasive detection of materials. However, the development of propagation techniques is relatively slow in comparison with the development of sources and detectors. The reason is that the propagation loss of millimeter/THz-wave in free space is higher than the propagation of microwave because millimeter/THz-wave can be highly absorbed to water vapor and oxygen in atmosphere. Furthermore, the scattering of millimeter/THz-waves by impedance mismatching between waveguide (an antenna with source) and free space also disturbs propagation of waves. From this, we consider that low-loss transmission techniques in free space should be developed for these problems as well as development of sources and detectors. To solve this, Goldsmith introduce quasi-optics for design transmission systems easily [1]. In quasi-optics, we can define millimeter/THz wave to Gaussian beam based on paraxial approximation and linear polarized state. Then, beam transformation can be applied to quasi-optical systems for design analytical beam path. The quasi-optical mirror and lenses can be used as reprehensive tools of low loss transmission system. Recently, quasi-optical transmission system is widely used for measuring complex permittivity



of dielectric materials for THz applications [2]–[4]. Nevertheless, measuring conducting media in quasi-optical system is still not common despite quasi-optics have an advantage as measurement system. From this reason, we present developed measuring technique of complex permittivity in conducting media such as semi-conductor and plasma. Furthermore, we proposed appropriate modeling of plasma density and carrier density in semi-conductor within quasi-optical millimeter- and THz-wave system. Based on these techniques, we also developed their applications such as measuring carrier lifetime of semiconductor for defect observation and plasma diagnostics of high-density inductively coupled plasma (ICP). In addition, a fast control of high-power millimeter-wave using pulsed plasma will be discussed in this thesis.

## 1.2 Thesis outline

The theory of quasi-optical millimeter- and THz-wave systems will be reviewed in chapter 2 with the theory of EM wave propagation in lossy media having complex permittivity. Definition of gaussian beam with quasi-optical mirror, mode matching for Gaussian beam transformation and oversized corrugated waveguide for HE<sub>11</sub> mode transmission will be discussed in this section. In chapter 3 and 4, the comprehensive applications of quasi-optical technique will be discussed with concepts of measurement system of material characterization having complex permittivity. As a comprehensive technique of millimeter- and THz-wave, the quasi-optical photoconductivity decay (QO-PCD) will be introduced for measuring carrier lifetime in semi-conductor as described in Chapter 3. The design of quasi-optical F-band (90~140 GHz) transmission system for high-density plasma diagnostics with proposed two-dimensional (2D) plasma density model will be discussed in Chapter 4. The experimental results of the plasma switching system in cold test using vector network analyzer (VNA) and hot test using kilo-watt level gyrotron (95 GHz, 20 us) will be discussed the remainder of Chapter 4. Finally, the conclusions are given Chapter 5.

# Chapter 2

## Concept of quasi-optical transmission system in millimeter- and THz-waves

### 2.1 Low loss quasi-optical transmission system

#### 2.1.1 Gaussian beam using corrugated horn antenna

A millimeter- and THz-waves can be propagated to free space with analytic solution which called quasi-optics [1]. The quasi-optical system is very important for low loss transmission of electromagnetic (EM) wave following Gaussian distributed field profile. A Gaussian beam is used as an analytical solution of wave equation in free space or a complex media. To treat a problem of diffraction in THz region, largely collimated wave is applied to gaussian beam optics. To derivative a solution of wave equation, a component,  $\psi$ , of EM wave follow that the Helmholtz equation is a kind of partial differential equation for the description of a time independent wave propagation.

$$(\nabla^2 + k^2)\psi = 0 \quad (1)$$

Where  $\psi$  represent any component of  $\mathbf{E}$  or  $\mathbf{H}$ . The wave number  $k$  is equal to  $2\pi/\lambda$ .  $\lambda$  is wavelength. When  $u$  is a complex scalar function that defines the non-plane wave part of the beam. In rectangular coordinates, the Helmholtz equation is

$$\frac{\partial^2 E}{\partial x^2} + \frac{\partial^2 E}{\partial y^2} + \frac{\partial^2 E}{\partial z^2} + k^2 E = 0 \quad (2)$$

If we apply quasi-plane wave solution, we can express

$$\frac{\partial^2 u}{\partial x^2} + \frac{\partial^2 u}{\partial y^2} + \frac{\partial^2 u}{\partial z^2} - 2jk \frac{\partial u}{\partial z} = 0 \quad (3)$$

The paraxial approximation,  $[\Delta(\partial u/\partial z)/\Delta z]\lambda \ll \partial u/\partial z$ , can be applied to wave equation. Finally, the third terms can be ignored compared with first and second terms.

$$\frac{\partial^2 u}{\partial x^2} + \frac{\partial^2 u}{\partial y^2} - 2jk \frac{\partial u}{\partial z} = 0 \quad (4)$$

It called paraxial wave equation in rectangular coordinates. For practical situations having the axial symmetry (e.g., corrugated horn antenna, lenses and mirrors), We can express axially symmetric paraxial wave equation (6) from (5).

$$\frac{\partial^2 u}{\partial r^2} + \frac{1}{r} \frac{\partial u}{\partial r} + \frac{1}{r} \frac{\partial^2 u}{\partial \phi^2} - 2jk \frac{\partial u}{\partial z} = 0 \quad (5)$$

$$\frac{\partial^2 u}{\partial r^2} + \frac{1}{r} \frac{\partial u}{\partial r} - 2jk \frac{\partial u}{\partial z} = 0 \quad (6)$$

To find solution, the simplest solution of the axially symmetric paraxial wave equation can be expressed in (7)

$$u(r, z) = A(z) \exp \left[ \frac{-jkr^2}{2q(z)} \right] \quad (7)$$

Where  $A$  and  $q$  are two complex functions. As a complex beam parameter, it is reasonable to write  $\frac{1}{q} = \left(\frac{1}{q}\right)_r - j \left(\frac{1}{q}\right)_i$ , the exponential term becomes

$$\exp \left( \frac{-jkr^2}{2q} \right) = \exp \left[ \left( \frac{-jkr^2}{2} \right) \left( \frac{1}{q} \right)_r - \left( \frac{kr^2}{2} \right) \left( \frac{1}{q} \right)_i \right] \quad (8)$$

The imaginary term expresses the form of the phase variation produced by a spherical wave front in the paraxial limit. Phase variation  $\phi(r)$  and radius of curvature  $R$  can define Eq. (9) and Eq. (10) in the limit  $r \ll R$ .

$$\phi(r) \cong \frac{\pi r^2}{\lambda R} = \frac{kr^2}{2R} \quad (9)$$

$$\left( \frac{1}{q} \right)_r = \frac{1}{R} \quad (10)$$

In standard form for Gaussian distribution, Eq. (11)

$$f(r) = f(0) \exp \left[ - \left( \frac{r}{r_0} \right)^2 \right] \quad (11)$$

We see that the quantity  $r_0$  represents the distance to the 1/e point relative to the on-axis value. Imaginary part has this form we take

$$\left(\frac{1}{q}\right)_i = \frac{2}{kw^2(z)} = \frac{\lambda}{\pi w^2} \quad (12)$$

And thus define the beam radius  $w$ , which is the value of the radius at which the field falls to  $1/e$  relative to its on-axis value. With these definitions, we can express

$$\frac{1}{q} = \frac{1}{R} - \frac{j\lambda}{\pi w^2} \quad (13)$$

Where both  $R$  and  $w$  are functions of  $z$ .

At  $z=0$ ,  $u(r, 0) = A(0)\exp\left(\frac{-jkr^2}{2q(0)}\right)$  and  $w_0 = [\lambda q(0)/j\pi]^{0.5}$  can be defined as beam radius at  $z=0$ , which is called the beam waist radius  $w_0$ .

$$u(r, 0) = u(0,0)\exp\left(\frac{-r^2}{w_0^2}\right) \quad (14)$$

$$q = \frac{j\pi w_0^2}{\lambda} + z \quad (15)$$

From Eq. (15), Gaussian beam is defined by beam radius ( $w$ ) and radius of curvature ( $R$ ) written by

$$R = z + \frac{1}{z} \left(\frac{\pi w_0^2}{\lambda}\right)^2 \quad (16)$$

$$w = w_0 \left[1 + \left(\frac{\lambda z}{\pi w_0^2}\right)^2\right]^{0.5} \quad (17)$$

Using Eq. (16) and (17), we can express that the electric field of Gaussian beam is

$$\mathbf{E}(r, z) = E_0 \hat{x} \frac{w_0}{w(z)} \exp\left(\frac{-r^2}{w(z)^2}\right) \exp\left(-i\left(kz + k\frac{r^2}{2R(z)} - \psi(z)\right)\right) \quad (18)$$

Where  $E_0 = E(0,0)$ , the electric field amplitude (and phase) at the origin at time 0,  $\psi(z) = \arctan\left(\frac{z}{z_R}\right)$  is the Gouy phase at  $z$ , an extra phase term beyond that attributable to the phase velocity of light.  $z_R = \frac{\pi w_0^2}{\lambda}$  is the Rayleigh range. In other hands, the propagation of Gaussian beam follows geometric optics in macroscopic point of view. Therefore, we can transmit Gaussian beam to target point using dielectric lenses and metallic mirrors.

## 2.1.2 Quasi-optical mirror with mode matching technique

The advantage of quasi-optical mirror is that we can design path of the beam propagation with wanted beam size and position using geometrical optics. Considering an initial Gaussian beam is fixed by

aperture of corrugated feed horn antenna, we can design a quasi-optical mirror with wanted output beam size and beam position using mode matching theory [1].

$$\mathcal{M} = \frac{w_{0,out}}{w_{0,in}}$$

Where  $\mathcal{M}$  is ratio of an initial beam waist ( $w_{0,in}$ ) to an output beam waist ( $w_{0,out}$ ) from reflected mirror,  $d_i$  is an input distance from source to mirror surface. Based on  $w_{0,in}$ ,  $\mathcal{M}$  and  $d_i$ , we can find output distance  $d_o$  and the curvature of radius  $R_o$  from focal point to output beam waist using Eq. (19).

$$f_q = \begin{cases} z_c \left( \frac{d_i}{\eta z_c} \right) \left[ 1 \pm \left( 1 - \eta \left[ 1 + \left( \frac{d_i}{z_c} \right)^{-2} \right] \right)^{0.5} \right], & \mathcal{M} \neq 1, \eta = 1 - \mathcal{M}^{-2} \\ z_c \frac{1 + \left( \frac{d_i}{z_c} \right)^2}{2 \left( \frac{d_i}{z_c} \right)}, & \mathcal{M} = 1, \end{cases} \quad (19)$$

$$R_o = \left( \frac{1}{f_q} - \frac{1}{R_i} \right)^{-1} \quad (20)$$

$$z_c = \frac{\pi w_0^2}{\lambda} \quad (21)$$

The quasi-optical off-axis ellipsoidal mirror is defined by

$$\frac{x^2}{a^2} + \frac{y^2 + z^2}{b^2} = 1 \quad (22)$$

$$a = \frac{R_i + R_o}{2} \quad (23)$$

$$b = \sqrt{R_i R_o \cos^2 \left( \frac{\theta}{2} \right)} \quad (24)$$

Where  $\theta$  is the angle between the initial beam and the output beam

The quasi-optical off-axis parabolic mirror is defined by

$$\rho = \frac{2f_p}{1 + \cos\theta} = f_p(\theta = 2\theta_i), \quad (25)$$

$$z' = \frac{y'^2}{4\rho \cos\theta_i} + \frac{x'^2 \cos\theta_i}{4\rho}, \quad (26)$$

Where  $\rho$  is a distance from focal point to mirror surface,  $f_p$  is the focal length,  $(x', y', z')$  is “local” coordinate system.

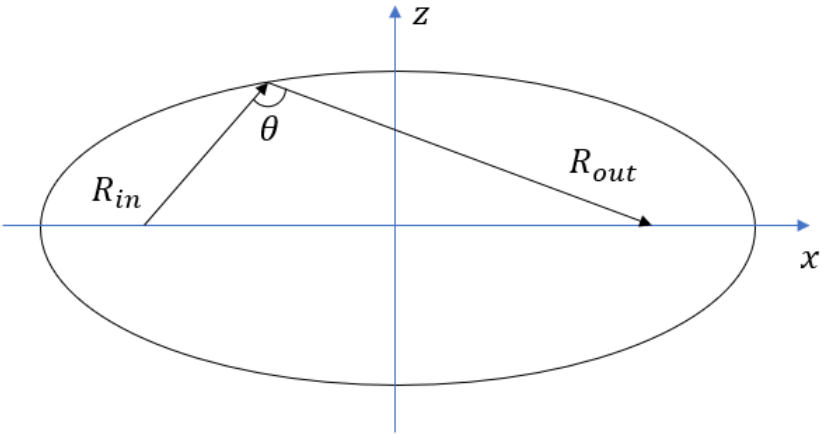


Figure 2-1. Geometry of quasi-optical ellipsoidal mirror

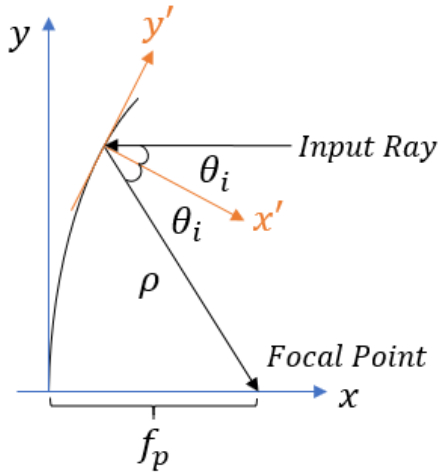
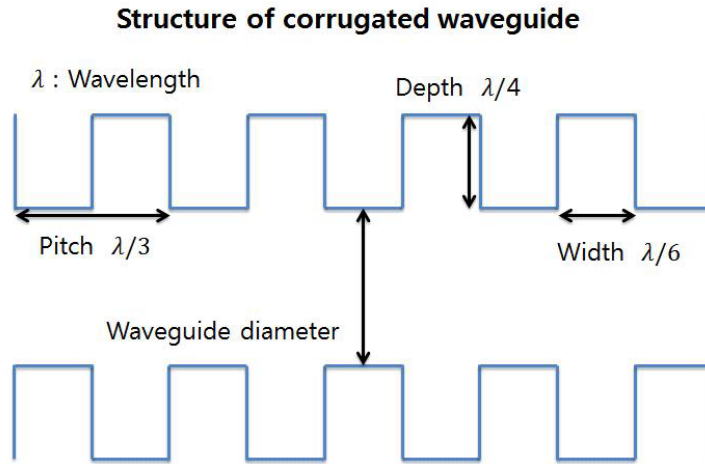


Figure 2-2. Geometry of quasi-optical parabolic mirror

### 2.1.3 Oversized corrugated waveguide for HE<sub>11</sub> mode transmission

The oversized corrugated waveguide is necessary to transmit high-power EM waves in low loss. The structure parameters are made up by corrugated depth ( $d_\lambda$ ) and pitch  $p_\lambda$ . To reduce ohmic loss in corrugated waveguide, the diameter of waveguide should larger than wavelength ( $D/\lambda \gg 1$ ,  $D$  is diameter of waveguide). Impedance matching condition should be followed by



**Figure 2-3.** Structure of corrugated waveguide

$$Z_\lambda = \frac{w_\lambda}{p_\lambda} \tan(kd_\lambda) \quad (27)$$

$$d_\lambda = \frac{\lambda}{4} \quad (28)$$

The hybrid modes consisting of TE modes and TM modes is propagated in corrugated waveguide. The field equations are defined by

$$E_x(r, \phi) = \frac{\sqrt{2Z_0}}{R\sqrt{\pi_1}} \cdot \frac{J_{m-1}\left(\frac{\chi_{m,n}r}{R_w}\right)}{J'_{m-1}(\chi_{m,n})} \cos[(m-1)\phi] \quad (29)$$

$$E_y(r, \phi) = \frac{\sqrt{2Z_0}}{R\sqrt{\pi_1}} \cdot \frac{J_{m-1}\left(\frac{\chi_{m,n}r}{R_w}\right)}{J'_{m-1}(\chi_{m,n})} \sin[(m-1)\phi] \quad (30)$$

Eq. (29) and Eq.(30) is  $HE_{mn}$  modes,  $m$  is radial number,  $n$  is azimuthal number,  $\chi_{m,n}$  is eigenvalue of Bessel function ( $J_{m-1}(x)=0$  in HE mode,  $J_{m+1}(x)=0$  in EH mode),

$$E_x(r, \phi) = \frac{\sqrt{2Z_0}}{R\sqrt{\pi_1}} \cdot \frac{J_{m+1}\left(\frac{\chi_{m,n}r}{R_w}\right)}{J'_{m-1}(\chi_{m,n})} \cos[(m+1)\phi] \quad (31)$$

$$E_y(r, \phi) = \frac{\sqrt{2Z_0}}{R\sqrt{\pi_1}} \cdot \frac{J_{m+1}\left(\frac{\chi_{m,n}r}{R_w}\right)}{J'_{m-1}(\chi_{m,n})} \sin[(m+1)\phi] \quad (32)$$

**Table 1.** Mixed field components in HE11 modes

TE modes	$TE_{11} \begin{cases} 84.496\% \\ 0^\circ \end{cases}$	$TE_{12} \begin{cases} 0.082\% \\ 180^\circ \end{cases}$	$TE_{13} \begin{cases} 3.58 \times 10^{-3}\% \\ 180^\circ \end{cases}$	$TE_{14} \begin{cases} 4.94 \times 10^{-4}\% \\ 180^\circ \end{cases}$
TM modes	$TM_{11} \begin{cases} 14.606\% \\ 0^\circ \end{cases}$	$TM_{12} \begin{cases} 0.613\% \\ 0^\circ \end{cases}$	$TM_{13} \begin{cases} 0.121\% \\ 0^\circ \end{cases}$	$TM_{14} \begin{cases} 0.039\% \\ 0^\circ \end{cases}$

Eq. (31) and Eq.(32) is  $EH_{mn}$  modes,  $R_w$  is a radius of waveguide and  $Z_0$  is impedance in free space.

The fundamental mode,  $HE_{11}$ , should be dominated in waveguide for radiation of gaussian beam from aperture of antenna. The Table show configuration of  $HE_{11}$  mode. The Figure 2-4 shows that field pattern of TE and TM modes. The Figure 2-5 and the Figure 2-6 show field pattern of hybrid modes.

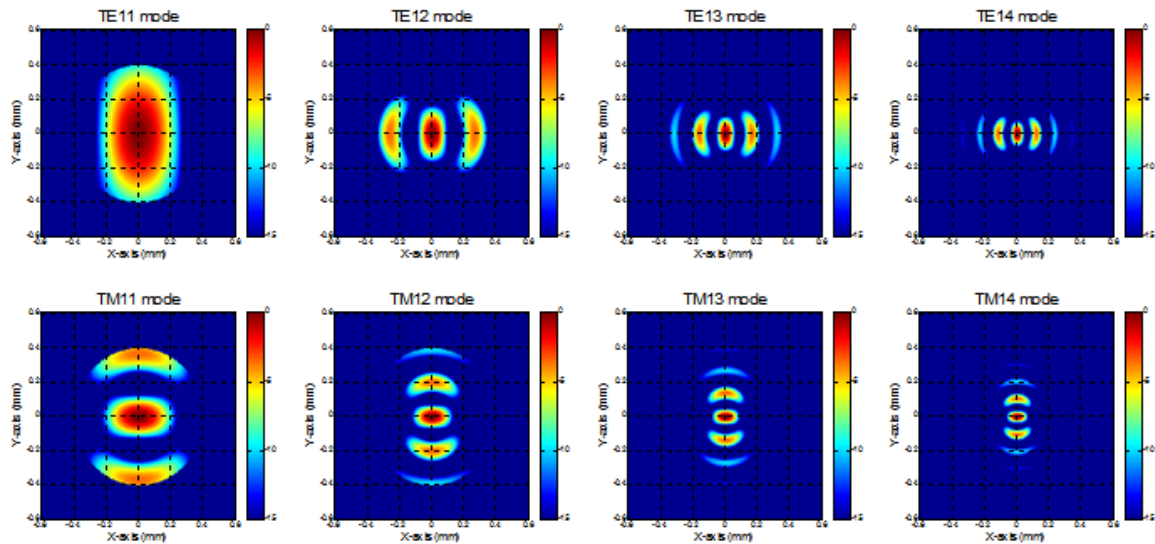


**Figure 2-4.** Electric field patterns of each TE and TM modes in hybrid modes



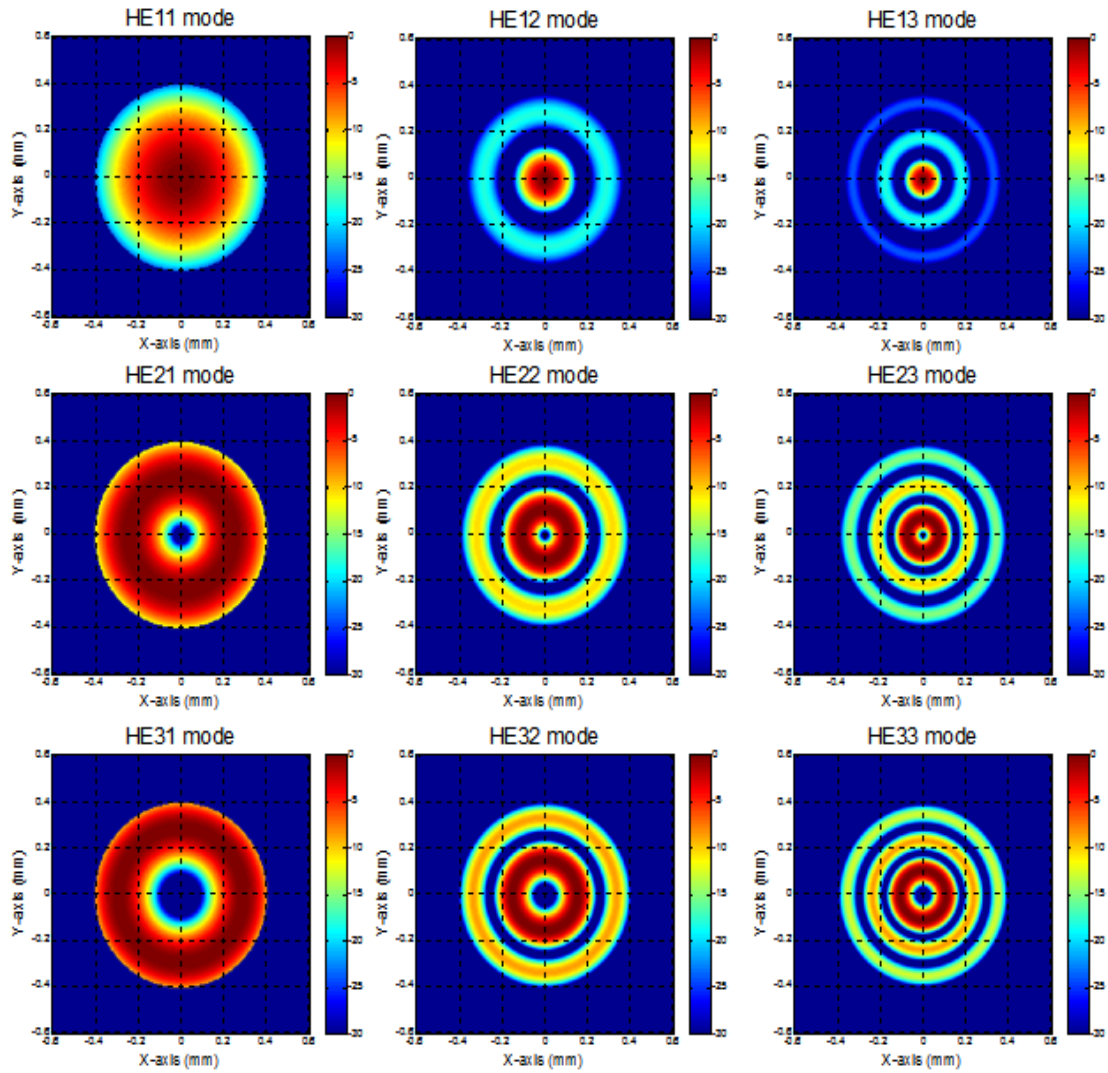


Figure 2-5. Higher order modes in HE mode

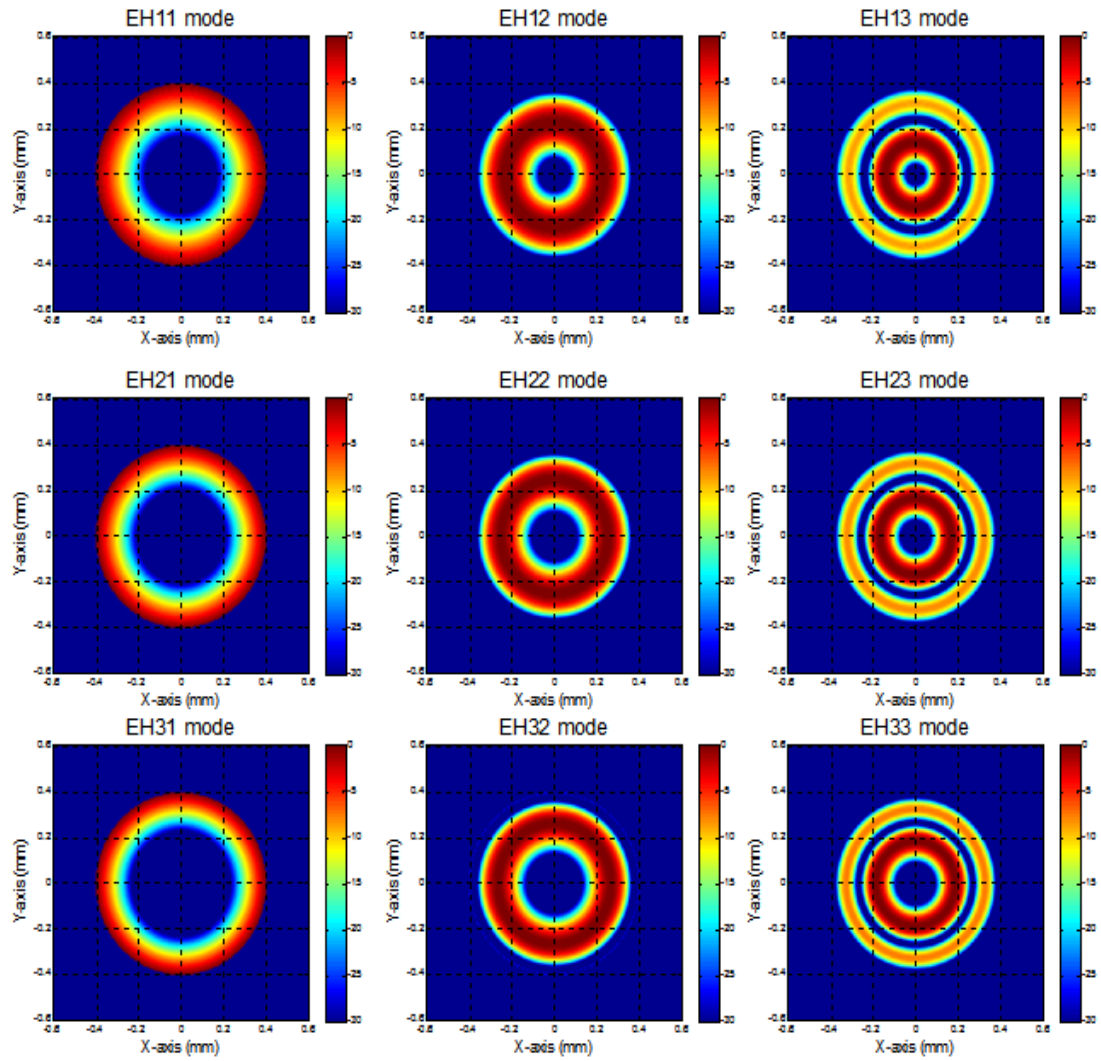
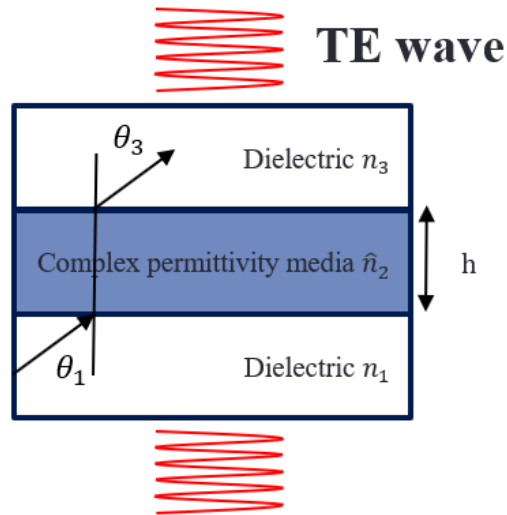


Figure 2-6. Higher order modes in EH mode

## 2.2 Theory of complex permittivity measurement using quasi-optical technique



**Figure 2-7.** A photo-excited media between two dielectric media

Transmittance and reflectance and absorption of EM wave in complex media (semi-conductor and plasma layer) is essential for diagnose permittivity of the complex media. According to the theory of absorbing films in optics [5], When a transverse electric (TE) wave go through three-layered media, we can express

$$\hat{n}_2 = n_2(1 + i\kappa_2) \quad (17)$$

It is convenient to set

$$\hat{n}_2^2 \cos\theta_2 = u_2 + iv_2 \quad (18)$$

where  $u_2$ ,  $v_2$  are real. We can easily express  $u_2$  and  $v_2$  in terms of the angle of incidence and the constants which characterize the optical properties of the first and the second medium.  $\hat{n}_2$  is a complex refractive index,  $n_i$  is a refractive index,  $\kappa_2$  is an attenuation index,  $\theta_i$  is an incident angle.

$$(u_2 + iv_2)^2 = \hat{n}_2^2 - n_1^2 \sin^2\theta_1 \quad (19)$$

$$u_2^2 - v_2^2 = n_2^2(1 - \kappa_2^2) - n_2^2 \sin^2\theta_1 \quad (20)$$

$$u_2 v_2 = n_2^2 \kappa_2 \quad (21)$$

$$2u_2^2 = \hat{n}_2^2(1 - \kappa_2^2) - n_1^2 \sin^2 \theta_1 + \sqrt{[\hat{n}_2^2(1 - \kappa_2^2) - n_1^2 \sin^2 \theta_2]^2 + 4n_2^4 \kappa_2^2} \quad (22)$$

$$2v_2^2 = -[\hat{n}_2^2(1 - \kappa_2^2) - n_1^2 \sin^2 \theta_1] + \sqrt{[\hat{n}_2^2(1 - \kappa_2^2) - n_1^2 \sin^2 \theta_2]^2 + 4n_2^4 \kappa_2^2} \quad (23)$$

$$r_{12} = \rho_{12} e^{i\phi_{12}} = \frac{n_1 \cos \theta_1 - (u_2 + iv_2)}{n_1 \cos \theta_1 + (u_2 + iv_2)} \quad (24)$$

$$t_{12} = \tau_{12} e^{i\chi_{12}} = \frac{2n_1 \cos \theta_1}{n_1 \cos \theta_1 + u_2 + iv_2} \quad (25)$$

$$\rho_{12}^2 = \frac{(n_1 \cos \theta_1 - u_2)^2 + v_2^2}{(n_1 \cos \theta_1 + u_2)^2 + u_2^2} \quad (26)$$

$$\tan \phi_{12} = \frac{2v_2 n_1 \cos \theta_1}{u_2^2 + v_2^2 - n_1^2 \cos^2 \theta_1} \quad (27)$$

$$\rho_{23}^2 = \frac{(n_3 \cos \theta_3 - u_2)^2 + v_2^2}{(n_3 \cos \theta_3 + u_2)^2 + u_2^2} \quad (28)$$

$$\tan \phi_{23} = \frac{2v_2 n_3 \cos \theta_3}{u_2^2 + v_2^2 - n_3^2 \cos^2 \theta_3} \quad (29)$$

$$\tau_{12}^2 = \frac{(2n_1 \cos \theta_1)^2}{(n_1 \cos \theta_1 + u_2)^2 + v_2^2} \quad (30)$$

$$\tan \phi_{12} = \frac{2v_2 n_1 \cos \theta_1}{u_2^2 + v_2^2 - n_1^2 \cos^2 \theta_1} \quad (31)$$

$$\tau_{23}^2 = \frac{4(u_2^2 + v_2^2)}{(n_3 \cos \theta_3 + u_2)^2 + v_2^2} \quad (32)$$

$$\tan \chi_{23} = \frac{v_2 n_3 \cos \theta_3}{u_2^2 + v_2^2 + u_2 n_3 \cos \theta_3} \quad (33)$$

where  $\rho_{ij}$ ,  $\tau_{ij}$  is the amplitude and  $\phi_{ij}$ ,  $\chi_{ij}$  is the phase change for explicit expressions.

$$\eta = \frac{2\pi}{\lambda_0} h \quad (34)$$

where  $\lambda_0$  is a wavelength of TE wave and  $h$  is thickness of absorbing film.

$$\mathcal{R} = |r|^2 = \frac{\rho_{12}^2 e^{2v_2 \eta} + \rho_{23}^2 e^{-2v_2 \eta} + 2\rho_{12} \rho_{23} \cos[\phi_{23} - \phi_{12} + 2u_2 \eta]}{e^{2v_2 \eta} + \rho_{12}^2 \rho_{23}^2 e^{-2v_2 \eta} + 2\rho_{12} \rho_{23} \cos[\phi_{12} + \phi_{23} + 2u_2 \eta]} \quad (35)$$

$$\mathcal{J} = \frac{n_3 \cos \theta_3}{n_1 \cos \theta_1} |t|^2 = \frac{n_3 \cos \theta_3}{n_1 \cos \theta_1} \frac{\tau_{12}^2 \tau_{23}^2 e^{-2v_2 \eta}}{1 + \rho_{12}^2 \rho_{23}^2 e^{-4v_2 \eta} + 2\rho_{12} \rho_{23} e^{-2v_2 \eta} \cos[\phi_{12} + \phi_{23} + 2u_2 \eta]} \quad (36)$$

Using a refractive index and an attenuation index calculated from Drude-Zener model and single decay function, we can obtain time-transient transmittance and reflectance of TE wave in a semiconductor.

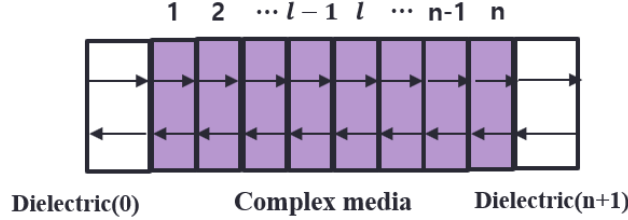


**Figure 2-8** Multi-layered complex media between dielectric media

The large scaled plasma thickness can be modeled as a multi-layered plasma and the EM wave propagation can be calculated using a propagation matrix method [5]. When the plasma layer comprises multiple layers, starting from  $l = 1$  to  $l = N$ , and the non-plasma layer is the free space at  $l = 0$  and  $l = N + 1$ , the boundary conditions can be represented by

$$\begin{bmatrix} A_{l+1} e^{-\kappa_{(l+1)z} e^{-ik_{(l+1)z} d_l}} \\ B_{l+1} e^{-\kappa_{(l+1)z} e^{ik_{(l+1)z} d_l}} \end{bmatrix} = \frac{1}{2} (1 + p_{(l+1)l}) \begin{bmatrix} 1 & R_{(l+1)l} \\ R_{(l+1)l} & 1 \end{bmatrix} \\ \times \begin{bmatrix} A_l e^{-\kappa_{(l+1)z} e^{-ik_{lz} d_l}} \\ B_l e^{-\kappa_{(l+1)z} e^{ik_{lz} d_l}} \end{bmatrix} = \bar{V}_{MN} \begin{bmatrix} A_l e^{-\kappa_{(l+1)z} e^{-ik_{lz} d_l}} \\ B_l e^{-\kappa_{(l+1)z} e^{ik_{lz} d_l}} \end{bmatrix}, \quad (48)$$

where

$$R_{(l+1)l} = \frac{[1 - p_{(l+1)l}]}{[1 + p_{(l+1)l}]}, \quad p_{(l+1)l} = \frac{[k_{lz}]}{[k_{(l+1)z}]} \quad (49)$$

$R_{(l+1)l}$  is the reflection coefficient at the boundary between the  $l^{\text{th}}$  and the  $l + 1^{\text{th}}$  regions;  $p_{(l+1)l}$  is the relative refractive index of the  $l^{\text{th}}$  and the  $l + 1^{\text{th}}$  regions;  $d_l$  is the position at the boundary between the  $l^{\text{th}}$  and the  $l + 1^{\text{th}}$ , and  $k_{lz}$  is the z-axis component of the angular wavenumber in the  $l^{\text{th}}$  region.  $A_l$  and  $B_l$  are the unknown amplitudes of reflected and transmitted waves. In Eq. (48), we can define the propagation matrix,  $\bar{V}_{MN}$ , for the boundary transition. At the  $(l + 1)^{\text{th}}$  region, we can express the propagation matrix,  $\bar{V}_{NP}$ , for the interior propagation in the same layer. From Eq. (48), we can derive the forward propagation matrix,  $\bar{V}_{(l+1)l}$ , from the  $l^{\text{th}}$  to the  $(l + 1)^{\text{th}}$  region.

$$\begin{aligned}
& \begin{bmatrix} A_{l+1}e^{-\kappa_{(l+1)z}}e^{-ik_{(l+1)z}d_{l+1}} \\ B_{l+1}e^{-\kappa_{(l+1)z}}e^{ik_{(l+1)z}d_{l+1}} \end{bmatrix} \\
&= \begin{bmatrix} e^{-\kappa_{(l+1)z}}e^{-ik_{(l+1)z}(d_{l+1}-d_l)} & 0 \\ 0 & e^{-\kappa_{(l+1)z}}e^{ik_{(l+1)z}(d_{l+1}-d_l)} \end{bmatrix} \begin{bmatrix} A_{l+1}e^{-\kappa_{(l+1)z}}e^{-ik_{(l+1)z}d_{l+1}} \\ B_{l+1}e^{-\kappa_{(l+1)z}}e^{ik_{(l+1)z}d_{l+1}} \end{bmatrix} \\
&= \bar{V}_{NP} \begin{bmatrix} A_{l+1}e^{-\kappa_{(l+1)z}}e^{-ik_{(l+1)z}d_l} \\ B_{l+1}e^{-\kappa_{(l+1)z}}e^{ik_{(l+1)z}d_l} \end{bmatrix} = \bar{V}_{NP} \cdot \bar{V}_{MN} \begin{bmatrix} A_l e^{-\kappa_{lz}} e^{-ik_{lz}d_l} \\ B_l e^{-\kappa_{lz}} e^{ik_{lz}d_l} \end{bmatrix} \\
&= \bar{V}_{(l+1)l} \begin{bmatrix} A_l e^{-\kappa_{lz}} e^{-ik_{lz}d_l} \\ B_l e^{-\kappa_{lz}} e^{ik_{lz}d_l} \end{bmatrix}. \tag{50}
\end{aligned}$$

Finally, the derived column matrix in the  $(N+1)^{\text{th}}$  region can be reorganized as

$$\begin{aligned}
\begin{bmatrix} 0 \\ T e^{ik_{(N+1)z}d_N} \end{bmatrix} &= \frac{1}{2}(1 + P_{(N+1)N}) \begin{bmatrix} 1 & R_{(N+1)N} \\ R_{(N+1)N} & 1 \end{bmatrix} \times \bar{V}_{N(N-1)} \cdots \bar{V}_{10} \begin{bmatrix} R e^{-ik_{0z}d_0} \\ e^{ik_{0z}d_0} \end{bmatrix} \\
&= \begin{bmatrix} v_{11} & v_{12} \\ v_{21} & v_{22} \end{bmatrix} \begin{bmatrix} R e^{-ik_{0z}d_0} \\ e^{ik_{0z}d_0} \end{bmatrix}. \tag{51}
\end{aligned}$$

Finally, by solving Eq. (51),  $R$  and  $T$  can be represented by

$$R = A_0/B_0 = -v_{12}e^{i2k_{0z}d_0}/v_{11}, \tag{52}$$

$$T = B_{N+1}/B_0 = (-v_{12}v_{21}e^{-ik_{0z}d_0}/v_{11} + v_{22}e^{-ik_{0z}d_0})e^{-ik_{N+1z}d_N}, \tag{53}$$

where  $R$  and  $T$  are the reflectance and the transmittance of the EM field in plasma, respectively.

# Chapter 3

## Measurement of the carrier lifetime in semi-conductor using a quasi-optical millimeter and THz waves

### 3.1 Concept of carrier lifetime measurement in semi-conductor

Based on THz-time domain spectroscopy (THz-TDS), a study of carrier dynamics in semiconductor has been studied in photonics as a THz application. To extend this application in electronics area, we developed carrier lifetime measurement technique in millimeter- and THz-wave regions. Originally, microwave is generally used as an EM probe of measuring minority carrier lifetime in semiconductor. The change of photoconductivity by optical pumping can be detected by response of the microwave because optical pumping excites carriers of semi-conductor from valence band to conduction band as shown in Figure 3-1. The Figure 3-2 show fundamental concepts of measuring carrier lifetime using EM wave. This method, the microwave photoconductivity decay method ( $\mu$ -PCD), has been used for the characteristics and two-dimensional scanning of silicon (Si) wafers [6]–[8]. The  $\mu$ -PCD method, which uses the microwave frequency range up to about 30 GHz, has many advantages, such as fast measurement, 2D mapping, and localized photoconductivity measurement. Nevertheless, this method has limitations because of the intrinsic characteristics in the microwave region. First of all, microwaves wavelength is longer than millimeter-wave, and the beam size (the beam size is determined to be the size of the beam whose intensity falls to  $1/e^2$  (corresponding to -8.7 dB) from the peak intensity [9]) for the microwave signal of the  $\mu$ -PCD antenna is relatively large ( $>100 \text{ mm}^2$ ) compared to the laser spot size ( $\sim 1 \text{ mm}^2$ ) for photoexcitation (Figure 3-4 and Figure 3-5). This limits the signal sensitivity for fine

regional mapping of the photoconductivity. Second, the microwave signal penetration is reduced in a thick silicon wafer ( $>100 \mu\text{m}$ ) in the case of a high doping density ( $> 10^{15}\text{cm}^{-3}$ ). In the microwave region, the Si sample reflectivity increases with the doping density, which leads to bad sensitivity with a thick sample as shown in Figure 3-3. This reduces the sensitivity. Therefore, detection a change in reflectance in a transient mode by using the existing  $\mu$ -PCD technique is difficult. The  $\mu$ -PCD method can measure a semiconductor with a low injection level and is applied under small perturbation conditions ( $\Delta\sigma \ll \sigma_0$ ) [7]–[9]. For low purity and low crystalline quality Si, the estimation of such wafers by using low-injection condition, that the  $\mu$ -PCD method is based on, is usually invalid due to the low signal to noise ratio and misreading of the measured lifetime out of its working condition [9]. At high injection levels, the relationship between the reflectivity and conductivity becomes nonlinear [8]. Thus, the measurement data are distorted, which may produce errors in the analysis of the photoconductivity decay time. In this study, we developed a technique called quasi-optical photoconductivity decay (QO-PCD) for measurement of a carrier lifetime of a sample by using an antenna and receiver in the millimeter- and terahertz (THz)-wave regime [10]. In these regimes, which cover frequencies between 100 GHz and 1 THz, there is a window for minimizing the reflectivity of thick samples or high doping densities. The reflectance above 100 GHz may be available for measuring samples with a high doped density because the reflectance is low enough to ensure high sensitivity measurements as compared to the reflectance in the microwave regime in  $\mu$ -PCD [11]–[13]. Furthermore, a Gaussian beam can be transmitted to a receiver with a beam waist size that can be reduced by increasing the frequency in the case of a quasi-optical system [1], [14], [15]. This means that the millimeter and terahertz waves have much better spatial resolution than microwaves, which allows the target region to be as small as  $1 \text{ mm}^2$ .

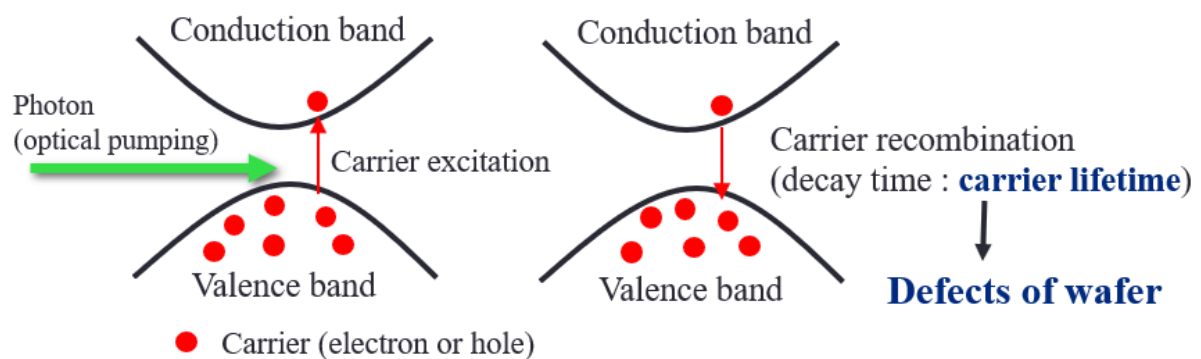
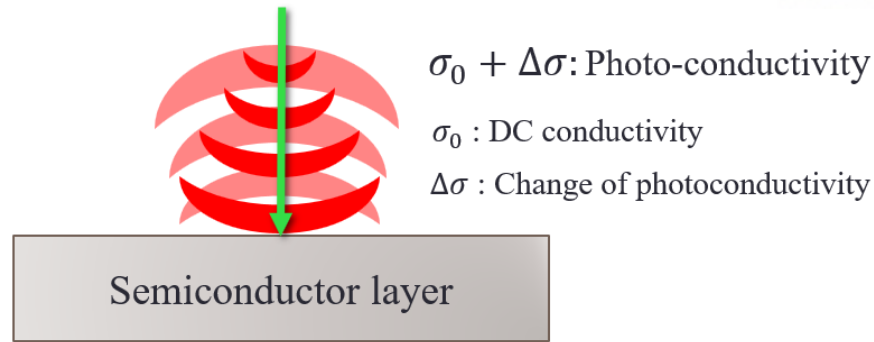


**Figure 3-1.** Carrier lifetime in semi-conductor





**Optical pumping** (  $\Delta\sigma$  : Change of photoconductivity )  
**Source & Detector** ( Detection of Reflectivity )

Figure 3-2. Concept of measuring carrier lifetime using EM wave

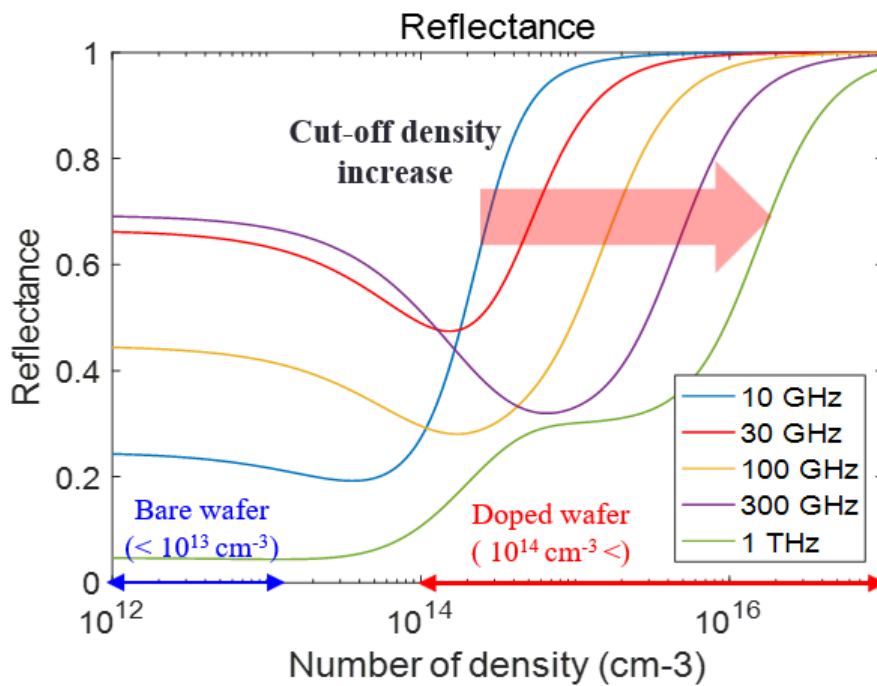
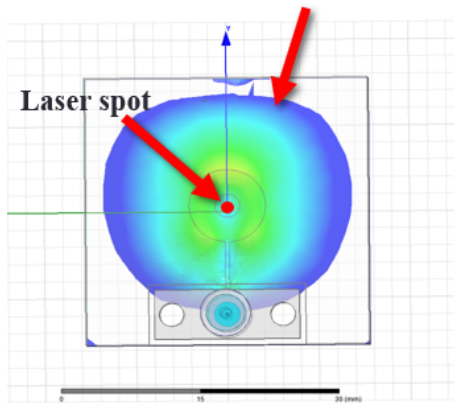


Figure 3-3. Reflectance of EM wave in semi-conductor

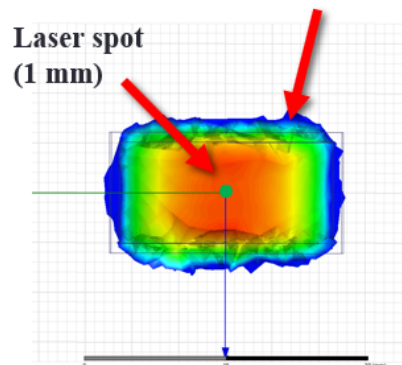
### Annular ring antenna

Field size  $\approx 30$  mm ( -8.7 dB )



### Waveguide antenna

Field size  $\approx 25$  mm ( -8.7 dB )



**HFSS simulation  
( FEM method )**

Figure 3-4. EM probes in u-PCD technique

**Millimeter wave  $\rightarrow$  THz-wave ( > 300 GHz )**

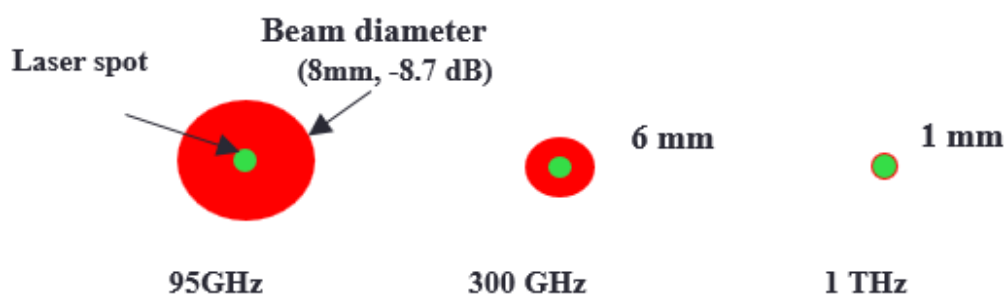


Figure 3-5. Beam size depending on frequency

## 3.2 Quasi-optical photoconductivity decay (QO-PCD) method

### 3.2.1 Theory of photoconductivity decay

The  $\mu$ -PCD technique search the minority carrier lifetime with the reflectance–conductivity relationship. In contrast, the quasi-optical transmission system does not use this principle. the transmittance and reflectance can be calculated in time domain based on the Zener–Drude model once the complex permittivity in the time domain is known [11], [12], [16]. A decay model of the carrier density can be defined as a fitting model for comparison with the experimental results [11]. Carriers in semi-conductor are made up by electrons and holes. The function of complex permittivity is defined by

$$\varepsilon = \varepsilon_{\infty} - \frac{\omega_{pe}^2}{\omega(\omega - iv_e)} - \frac{\omega_{ph}^2}{\omega(\omega - iv_h)} = \varepsilon_{\infty} + \left( i \frac{4\pi\sigma}{\omega} \right) \quad (54)$$

where  $\omega_{pe} = \sqrt{4\pi Ne/m_e^*}$  and  $\omega_{ph} = \sqrt{4\pi Ne/m_h^*}$  are the plasma frequencies of electrons and holes, respectively. The following relationships hold:  $v_e = 1/\tau_e, v_h = 1/\tau_h$ ,  $\tau_e = m_e^* \mu_e / e, \tau_h = m_h^* \mu_h / e$  ( $\mu_e$ : electron drift mobility,  $\mu_h$ : hole drift mobility,  $v_e$ : collision frequency of electrons,  $v_h$ : collision frequency of holes,  $\tau_e$ : carrier lifetime of electrons,  $\tau_h$ : carrier lifetime of holes,  $m_e^*$ : effective mass of electrons,  $m_h^*$ : effective mass of holes,  $N$ : carrier density,  $\omega$ : angular frequency,  $\varepsilon_{\infty}$ : dielectric constant of a material, and  $\sigma$ : conductivity).<sup>6</sup> The conductivity also contains complex terms represented by

$$\sigma(\omega) = \sigma_{dc}(\alpha + \beta i) = \frac{Ne^2}{m_e(v_e - i\omega)} + \frac{Ne^2}{m_h(v_h - i\omega)} \quad (55)$$

$$\sigma_{dc} = \frac{Ne^2}{m_e v_e} + \frac{Ne^2}{m_h v_h} \quad (\omega \ll v_e, v_h, 0) \quad (56)$$

where  $\sigma_{dc}$  is the DC conductivity. From Eq. (37) and Eq. (39), the refractive index  $n$  and attenuation index  $\kappa$  can be calculated for a semiconductor as follows:

$$n = \sqrt{\frac{\varepsilon_r}{2} + \sqrt{\left(\frac{\varepsilon_r}{2}\right)^2 + \left(\frac{\varepsilon_i}{2}\right)^2}}, \kappa = \sqrt{-\frac{\varepsilon_r}{2} + \sqrt{\left(\frac{\varepsilon_r}{2}\right)^2 + \left(\frac{\varepsilon_i}{2}\right)^2}} \quad (57)$$

where  $\varepsilon_r$  and  $\varepsilon_i$  are the real and imaginary parts of the complex dielectric function. Changes in the dc conductivity affect the refractive index and attenuation index. When a recombination is expressed as a decay function[8], [9], [17], the excess carrier density is represented by

$$N = n_0 \exp(-t/\tau_0) \quad (58)$$

where  $n_0$  is the initial excess carrier density in the conduction band and  $\tau_0$  is the initial exponential decay time constant. Based on the theory, we can simply simulated QO-PCD system as shown in Figure 3-6.

### Concepts of QO-PCD

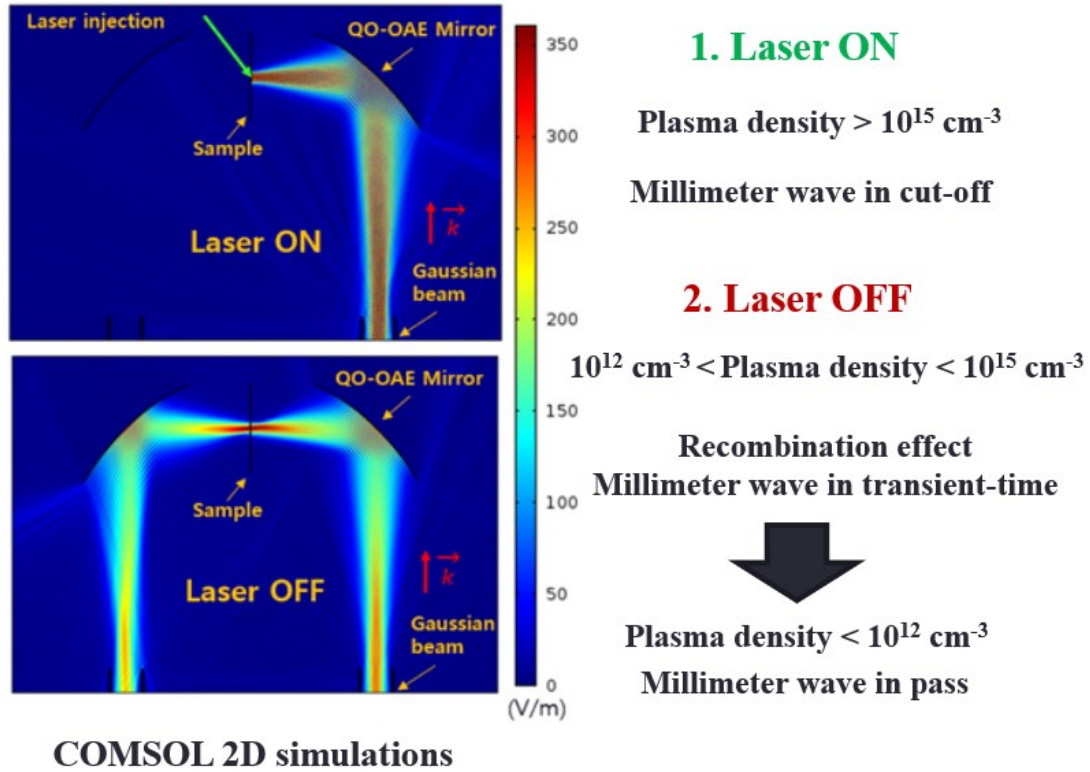


**Figure 3-6.** The path of gaussian beam with and without photo-excitations in 2D simulation (COMSOL Multiphysics)

### 3.2.2 Experimental setup of quasi-optical system

As a proof-of-concept experiment, we chose F-band millimeter-wave. In the experimental setup, a 95 GHz of Vector Network Analyzer (VNA, N5247A, Keysight Technologies) was used as a millimeter wave source with an amplifier (DET-10-RPNW1, Gain: 14 dB, Millitech Inc.). Figure 3-7 show the millimeter waves and optical pumping source (Nd: YAG laser, 532 nm, 15~18 ns, 0.27±0.02 W at 100 Hz repetition) in the quasi-optical transmission system. The beam size of optical pumping laser is approximately 1.57 mm in the full width at half maximum (FWHM). The Gaussian beam was transmitted from a corrugated feed horn to a wafer through a quasi-optical focusing mirror. The quasi-optical off-axis ellipsoidal (QO-OAE) mirror reflected the beam propagation direction by 90°. The 8 mm beam waist in the corrugated feed horn aperture was reduced by half at the wafer surface, corresponding to a  $16 \pi \text{ mm}^2$  area. This area is much smaller than the size of the WR90 standard waveguide ( $22.86 \times 10.16 \text{ mm}^2$ ) that is typically used with the  $\mu$ -PCD technique. The Figure 3-8 show

quasi-optical system is well designed by Surf3D simulation. Furthermore, phase of beam waist is almost flat at sample position and receiver position as shown in Figure 3-9 and Figure 3-10. Before the carrier lifetime was measured, the initial information for the Si sample was needed. This quasi-optical transmission system can measure the dielectric constant, thickness, and initial carrier density (dark conductivity) of Si sample by using the frequency sweep in VNA. Figure 3-11 shows free space measurement setup and Figure 3-12 shows the measured free space transmittance of quasi-optical system in the F-band (90–140 GHz). Finally, we can measure S21 parameter of Si in quasi-optical system as shown in Figure 3-13. The results agreed well with the theoretical model with a convergence error of around 1% based on Eq. 8. [3], [18], [19]. Note that the highest transmittance was obtained at 95 GHz.

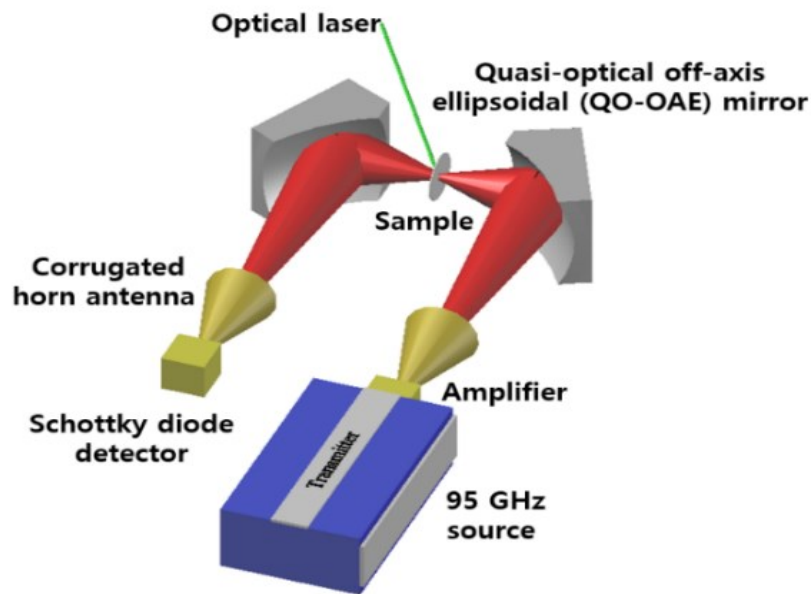


**Figure 3-7.** Schematic of QO-PCD

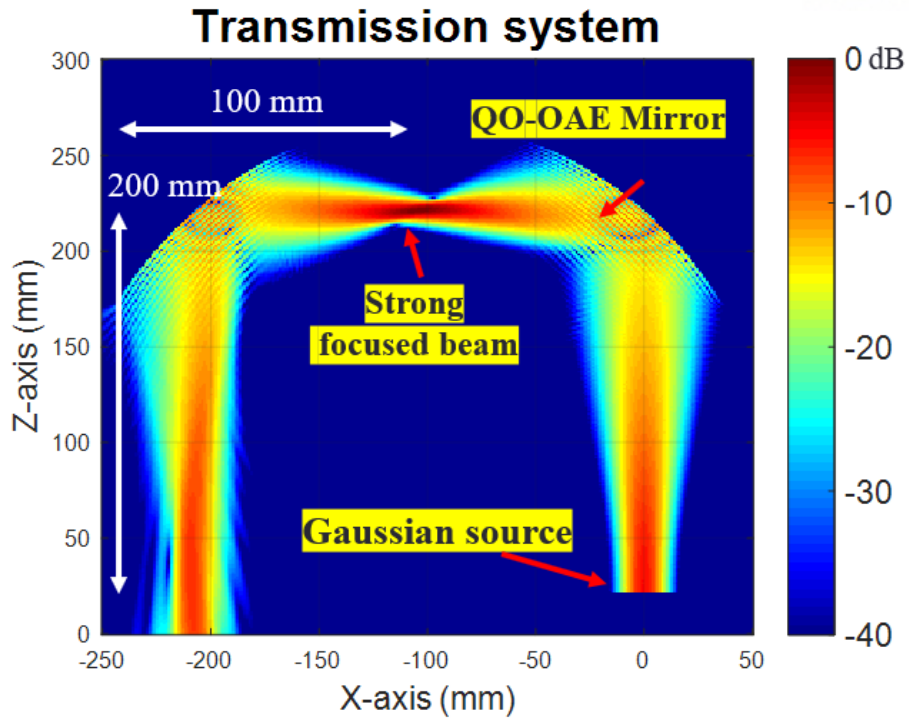


Figure 3-8. Quasi-optical transmission simulation using Surf3D code

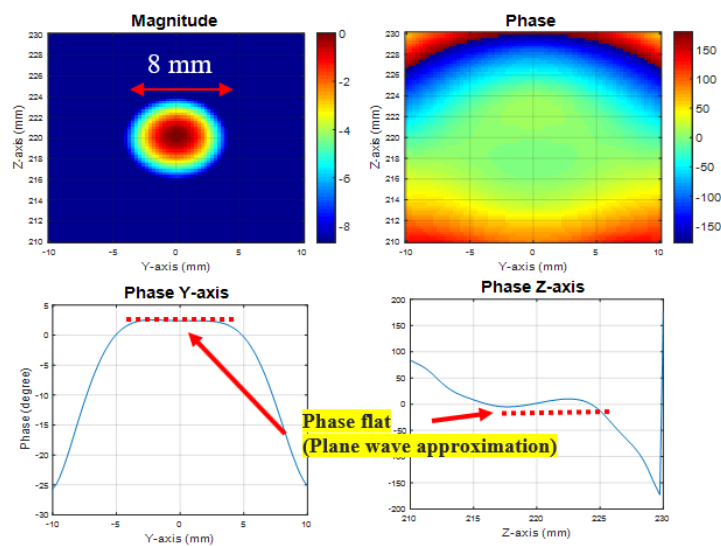


Figure 3-9 Surf3D results of Gaussian beam at sample position

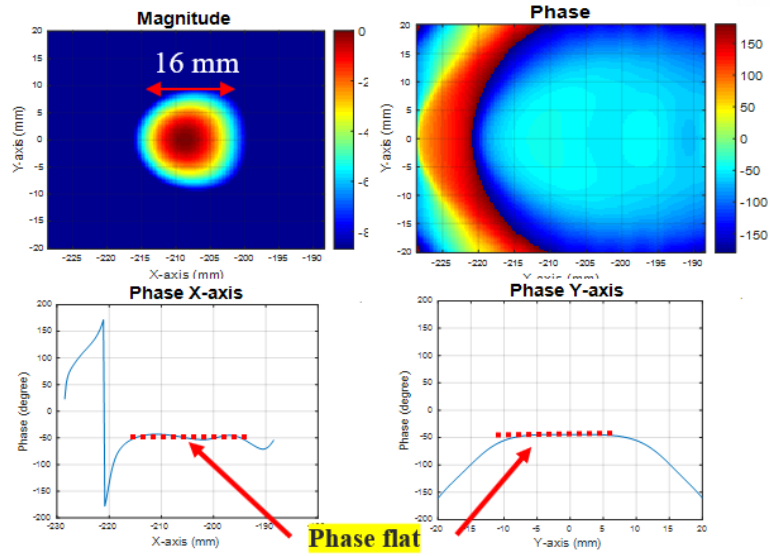


Figure 3-10. Surf3D results of Gaussian beam at receiver position

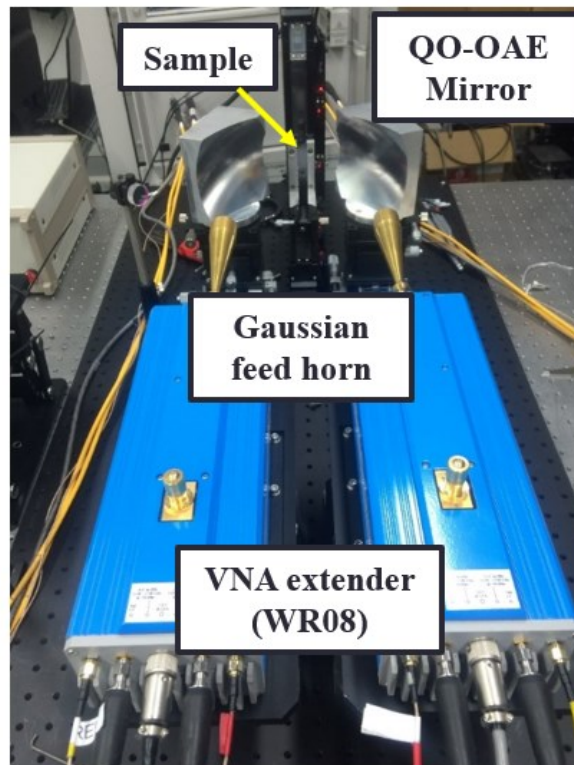
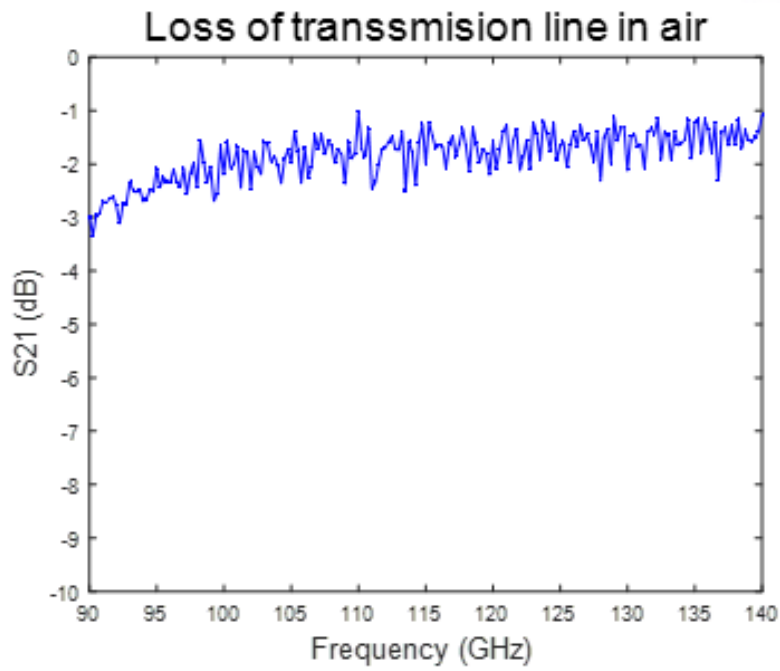
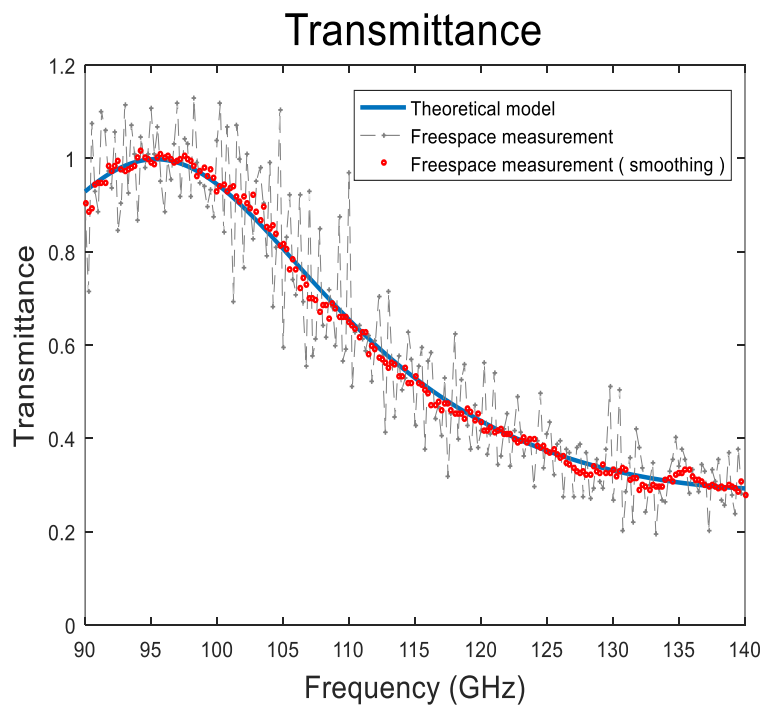


Figure 3-11. Free space permittivity measurement using quasi-optical system



**Figure 3-12.** Experimental result of free space loss in quasi-optical system



**Figure 3-13.** Transmittance results of semi-insulating Si wafer in QO transmission systems



**Table 2.** The specifications of 1<sup>ST</sup> QO-OAE mirror

Output beam distance	103.736mm
Input Radius curvature X-axis, Y-axis	106.1818 mm
Output Radius curvature X-axis, Y-axis	220.2975 mm

**Table 3.** The specifications of 2<sup>nd</sup> QO-OAE mirror

Frequency	95 GHz
Input beam waist	8 mm
Input beam distance	200 mm
Output beam waist from 1 <sup>st</sup> mirror (Strong focused beam)	4 mm ( $\lambda \sim 3.5$ mm)
Output beam waist from 2 <sup>nd</sup> mirror	8 mm

### 3.3 Experimental study of QO-PCD system

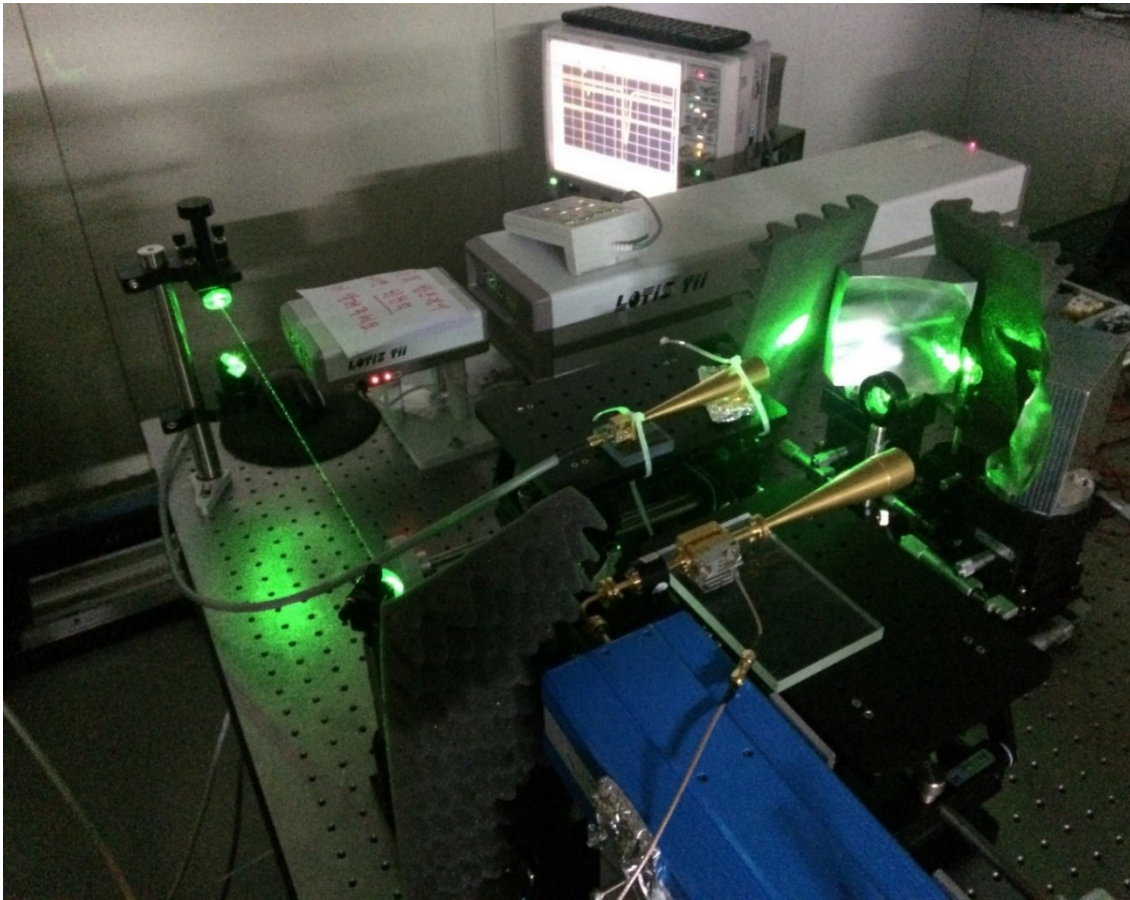


**Figure 3-14.** The experimental setup of QO-PCD

Finally, we measure carrier lifetime of Si sample in QO-PCD system. A Schottky diode detector was used to measure the radio-frequency (RF) signal with a fast response of as short as 1 ns. The detector was calibrated with a power meter (PM-5, Virginia Diode Inc.). By fitting the calibration data, we can convert the detector signal to a transmittance value. Figure 3-15 presents a time-resolved signal transmitted through excited semiconductor and measured by the Schottky diode detector with rough uncertainties (2% convergence error, laser power instability and detector calibration error). The detector signal suddenly falls down to zero when the optical pumping generates the free carriers on the Si. After the laser was turn off, the signal is penetrated to the wafer owing to carrier recombination. The excess carrier density and photoconductivity decay time were estimated as the decay model fitting results corresponding to the transmittance data, as presented in Table 4. To observe the defects distribution on the wafer, a configuration of 2D mapping system was installed for the QO technique. a 2D areal mapping of the photoconductivity decay time in auto-measurement system. For fast measurement, the rise time data of the detector signal was saved without calibration. The sampling points is 8100 pts. The detector signal was fitted linearly for calibration. The 2D image of the photo-excited carrier lifetime of

the Si wafer sample passivated by HF acid in Figure 3-16 (a). The error resulting from the non-ideal linear fitting curve shown in Figure 3-16 (b) was less than 10%. The 2D image shows that the carrier lifetime was distributed roughly. The important feature of the QO-PCD method is that the area under measurement can be focused to a small spot, which prevents the interference of unnecessary regions. Therefore, QO-PCD 2D mapping is trustworthy and provides high resolution. The QO-PCD technique is proved to measure a wide range of photoconductivity decay time change because the high sensitivity contributes to the high frequency measurement system, as described in Figure 3-16.

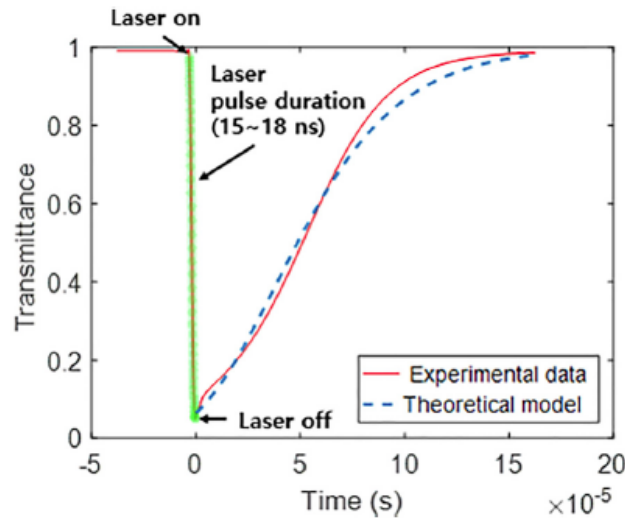


**Figure 3-15.** RF transmittance signal with optical pumping compared to the theoretical model.

**Table 4.** The experimental results of QO-PCD

<b>d (thickness)</b>	<b>460(±1) μm</b>
<b>ε<sub>0</sub> (dielectric constant)</b>	<b>11.65(±0.01)</b>
<b>n<sub>0</sub> (initial excess carrier density)</b>	<b>1.5(±0.01) × 10<sup>15</sup> cm<sup>-3</sup></b>
<b>τ<sub>0</sub> (carrier lifetime)</b>	<b>30.6 (±0.1) μs</b>

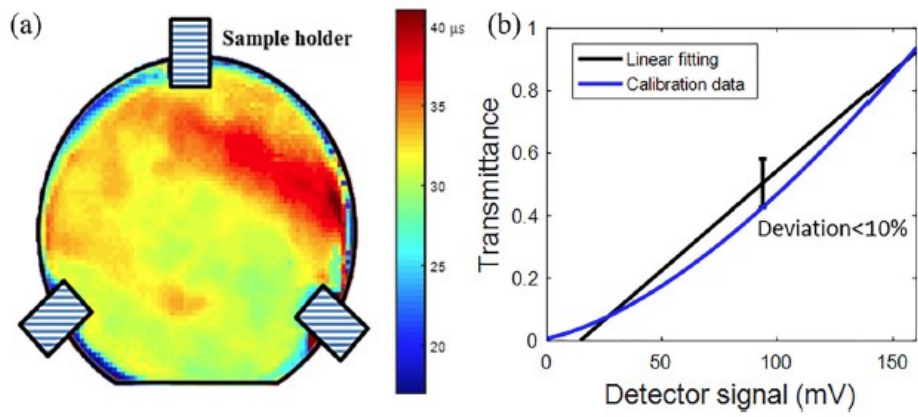


**Figure 3-16.** (a) 2D mapping results of carrier lifetime, (b) calibration error graph

# Chapter 4

## Characteristics of high-power millimeter-wave in pulsed plasma

### 4.1 Motivation

The suppression of neo-classical tearing modes (NTMs) which is one of plasma instability is a critical issue to prevent the disruption of H-mode plasma in fusion plasma tokamak. To operate steady-state drive, we should understand not only physical phenomena of tearing modes but also optimized conditions of electron cyclotron current drive (ECCD) to suppress time resolved NTMs in range of a few kHz repetition. We propose an external switching system which can be settled in existing transmission lines and gyrotrons. The idea of switching system simply comes from interactions between millimeter-wave and glow discharged cold plasma. The cut-off and propagation of millimeter-wave can be determined by the plasma switching. A helical type inductively coupled plasma chamber is designed for high transmission of Gaussian beam (linear polarized E-field having Gaussian profiled) and generation of high-density bulked plasma. For proof-of-concept study, we conducted cold test using vector network analyzer (low power millimeter-wave,  $< 1\text{mW}$ , continuous waves) and successfully demonstrated proto-type test of millimeter-wave switching having 2 kHz repetition. For hot test, a gyrotron at UNIST (95 GHz, few kW of power) is used as a high-power millimeter-wave source. Although the gyrotron pulse length (20  $\mu\text{s}$ ) is not enough to measure switching results (plasma switching time is 200  $\mu\text{s}$ ), we observed wave absorption in plasma and increase of plasma density simultaneously. This result will help to understand mechanism of millimeter wave heating in inductively coupled plasma. Furthermore, this study will also contribute to understand plasma instabilities in fusion plasma.

## 4.2 Design of inductive rf discharged high-density plasma

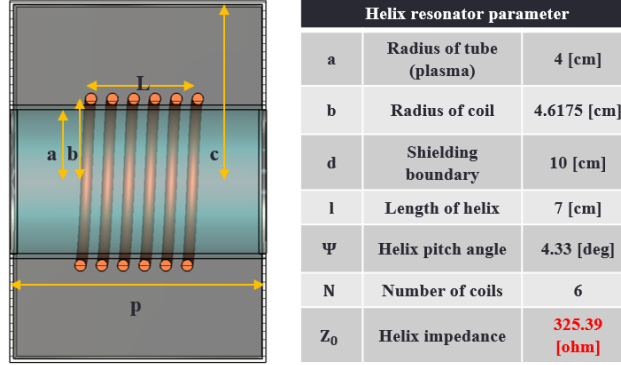


Figure 4-1. Helical structure of the ICP with designed parameters

An ICP chamber is designed to generate a high-density plasma with glow discharge based on the Liberman's helical resonator model [20]–[22]. The helix structure can generate cylindrical plasma based on helical slow wave modes between RF field and plasma. Dispersion relation can be derived from two-dimensional Helmholtz equation satisfying the axial field.

$$d^2 E_z / dx^2 - \beta^2 E_z + k^2 E_z = 0, \quad (59)$$

$$d^2 H_z / dx^2 - \beta^2 H_z + k^2 H_z = 0, \quad (60)$$

Where  $k = \omega / c_0$  is the free space wavenumber. Using axial-symmetry condition of cylindrical plasma, we can determine the fields, the dispersion relation, and the characteristic impedance easily.

The solutions are written by

$$E_{\theta a} = E_{\theta a} = -\frac{j\omega\mu}{2} \frac{c^2 - b^2}{c^2} K_{\theta} r, \quad (61)$$

$$E_{\theta c} = -\frac{j\omega\mu}{2} \frac{b^2}{c^2} K_{\theta} \frac{c^2 - r^2}{c^2 r}, \quad (62)$$

$$E_{rb} = \frac{-V}{r \ln(b/a)}, \quad (63)$$

$$E_{rc} = \frac{V}{r \ln(c/b)}, \quad (64)$$

$$E_{zb} = -\frac{p_0^2 V \ln(r/a)}{j\beta \ln(r/a)}, \quad (65)$$

$$E_{zc} = -\frac{p_0^2 V \ln(r/a)}{j\beta \ln(r/a)}, \quad (66)$$

Where  $K_{\theta} = H_{zb} - H_{zc}$ ,  $p_0^2 = \beta^2 - k^2$ ,  $V$  is the helix voltage amplitude.

The normal component of the displacement vector is continuous across the plasma-vacuum interface:

$$\varepsilon_p = \varepsilon_0 \left( 1 - \frac{\omega_p^2}{\omega(\omega + j\nu)} \right), \quad (67)$$

$$E_{ra}(r = a) = \frac{2\omega(\omega - j\nu)}{j\beta\omega_p^2 a} \frac{V}{\ln(b/a)}, \quad (68)$$

$$E_{zb} = -E_{\theta b} \cot\psi \text{ at } r = b$$

$$V = \frac{\omega\mu\beta}{2p_0^2} \frac{c^2 - b^2}{c^2} K_\theta b \cot\psi, \quad (69)$$

$$H_{\theta c} - H_{\theta b} = K_z = K_\theta \tan\psi, \quad (70)$$

$$K_\theta = V \frac{\omega\varepsilon_0}{\beta b} \left( \frac{1}{\ln(c/b)} + \frac{1}{\ln(b/a)} \right) \cot\psi, \quad (71)$$

Inserting (71) into (69) and using  $p_0^2$ , a relationship between the longitudinal component of a magnetic field and the generated plasma can be explained with a dispersion relation.

$$\beta^2 = g^2 k^2 \cot^2\psi, \quad (72)$$

where  $\beta$  is the axial wavenumber, and

$$g^2 = \frac{c^2 - b^2}{2c^2} \left[ \frac{1}{\ln(c/b)} + \frac{1}{\ln(b/a)} \right], \quad (73)$$

where  $g$  is the correction factor for a geometrical helix wave.  $\beta = g\beta_h$  and  $\beta_h$  are the axial wave numbers of the helix mode;  $k$  is the free-space wavenumber;  $\Psi = \tan^{-1}(L/4(N-1)b)$  is a helix pitch angle; and  $a$ ,  $b$ , and  $c$  are defined in Figure 4-1.

From the dispersion relation, we can calculate the characteristic impedance.

$$Z_0 = \zeta \sqrt{\frac{\mu_0}{\varepsilon_0}} \frac{Nb}{L}, \quad (74)$$

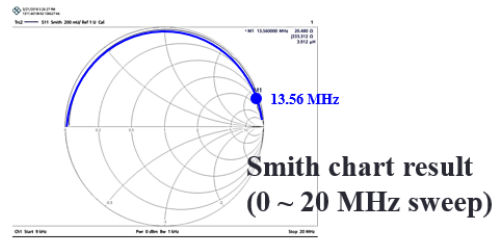
where

$$\zeta = \frac{g}{\frac{1}{\ln(c/b)} + \frac{1}{\ln(b/a)}} \quad (75)$$

is a geometrical factor.

The characteristic impedance of fabricated ICP chamber was measured by VNA and this result is well match to theoretical calculation in Figure 4-2.

### Impedance measurement by VNA



**Impedance :20.480+j333.312[Ω] |Z|=333.9286 [Ω]**  
**Inductance: 3.912[μH] at 13.56MHz**

Figure 4-2. Impedance measurement of ICP chamber (Frequency sweep: 0 ~ 20 MHz)



## 4.3 Experimental setup of Plasma switching system

### 4.3.1 Experimental setup

The Gaussian beam is injected into plasma layers by quasi-optical off-axis parabolic (QO-OAP) mirrors, such that the Gaussian beam is incident perpendicularly to the plasma surface. A pair of Gaussian F-band (90–140 GHz) horn antennas with a beam waist of 8 mm was used. The designed mirror was verified using a Surf3D simulation, as shown in Figure 4-3(a) [23]–[25]. The parallel Gaussian beam is propagated to a second mirror (QO-OAP Mirror 2,  $x = 175$  mm) reflected from the first one, and the beam size (radius) is maintained around 19 mm in all planes, as shown in Figure 4-3(a). The aluminum mirrors were fabricated with a 5-axis CNC machine and aligned using micrometer positioning in XYZ stages and rotation angle stages. Loss in the quasi-optical transmission system was measured with a VNA (Keysight technologies Inc., N5247A) with millimeter wave heads (OML Inc., WR08, F-band: 90–140 GHz), and the result is shown in Fig. 4-4(a). The transmission loss of the quasi-optical system is approximately -0.5 dB, which guarantees detection of plasma transmission loss with a high SNR. The experimental setup comprises the ICP system and the quasi-optical millimeter-wave system as described in Fig. 4-5. The final plasma radius and the Gaussian beam radius are 40 and 19 mm, respectively, guaranteeing the electromagnetic (EM) field having a -40 dB loss in the Gaussian beam profile for penetrating the plasma chamber. The quartz windows are designed for a high electromagnetic wave transmission at a target frequency of 95 GHz. The dielectric constant and the loss tangent of the quartz window are measured to be approximately 3.824 and  $4 \times 10^{-4}$ , respectively, with a thickness of 8.03 mm. These two quartz windows exhibit a transmittance of approximately 92% at 95 GHz. The RF coil surrounds the cylindrical quartz tube, which can confine the plasma. The edge of the tube is connected to the quartz windows for a high efficiency millimeter-wave transmission. To generate plasma, RF power is supplied by an RF generator (cito Plus 1310, PCT Comet Inc., 500–1,000 W at 13.56 MHz) with an impedance matching box. Argon (Ar) gas is injected into the plasma chamber in a range of 2–5 Torr using a mass-flow controller (MFC) (FC280 model, Tylan Inc.).

Successful Ar plasma operation with inductive rf discharge is shown in Figure 4-5(c). We measure the transmission signal ( $S_{21}$ ) at various RF power levels and gas pressures. Fig. 4-6 shows the transmittance results ( $S_{21}$ ) when the Gaussian beam is injected to Ar plasma when RF power and gas pressures vary. The plasma cut-off frequency tends to increase with the RF power and gas pressure in the frequency domain. From the experimental results, the plasma density and the effective collision frequency can be analyzed. For data analysis, we assume that the plasma follows the Drude model with a Maxwellian distribution from which the experimental results can be fitted to the theoretical model.

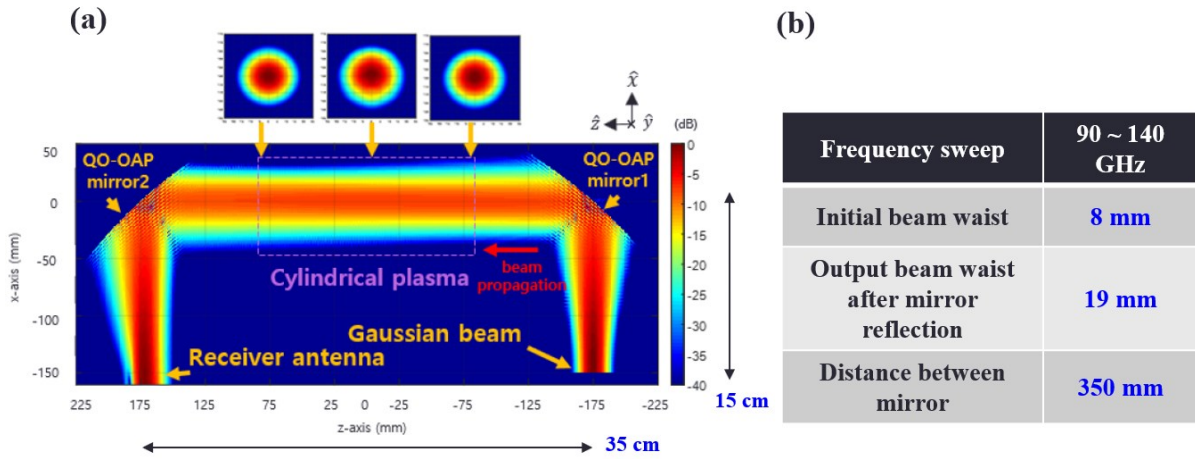


**Figure 4-3.** (a) Simulation results of QO-OAP mirrors using Surf3D code (b) Specifications of Gaussian beam in QO system.

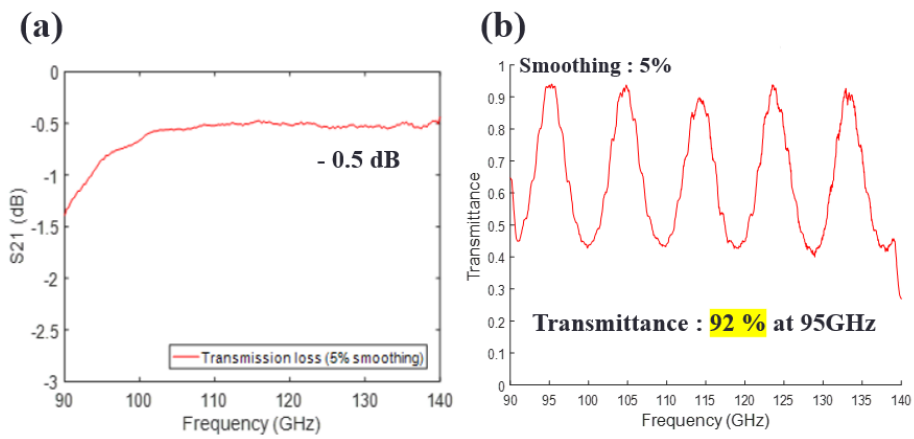


**Figure 4-4.** (a) Free space transmission loss in QO systems (5% smoothing) (b) Transmittance of two quartz windows in plasma chamber

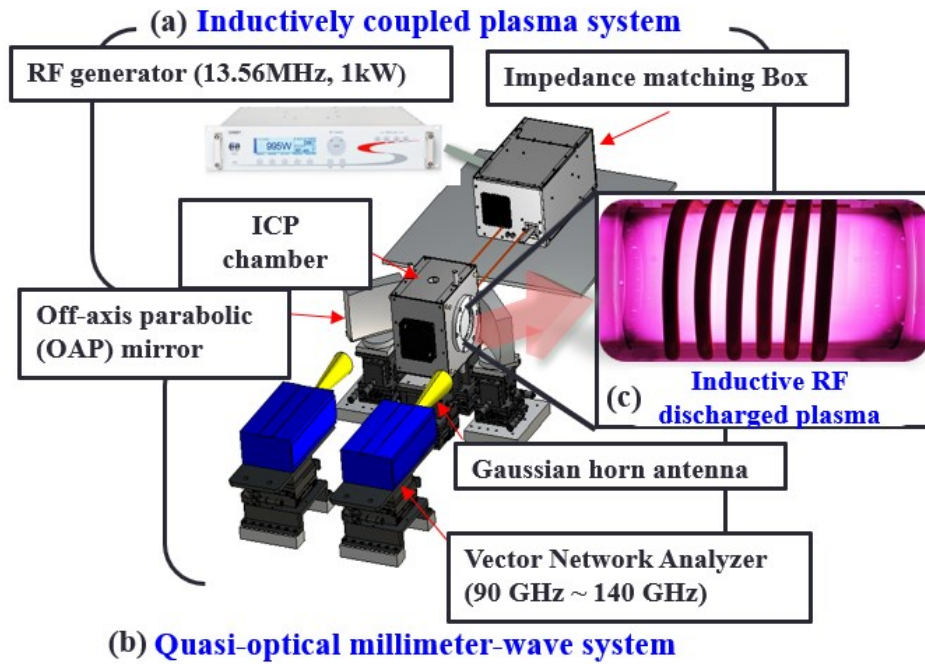


**Figure 4-5.** Schematic of ICP diagnosis using the quasi-optical millimeter-wave system: (a) ICP system; (b) quasi-optical millimeter-wave system; and (c) close-up of the experimental Ar ICP plasma (Pressure: 2 Torr, RF power: 1000 W)

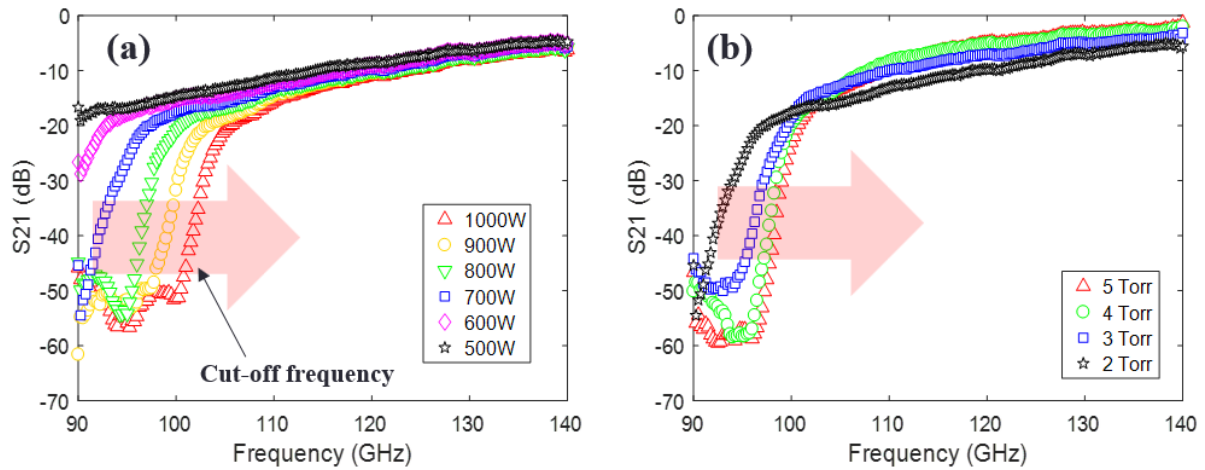


**Figure 4-6.** Experimental results of transmittance ( $S_{21}$ ) by EM-field penetrated from plasma: (a) RF power variations at 2 Torr; (b) pressure variations at 700 W

### 4.3.2 Analysis of pulsed plasma using non-invasive millimeter-wave

The EM wave propagation in plasma can be interpreted via spatial dispersion using classical electrodynamics [26]. Therefore, it is important to model the ICP plasma for the dispersion relation. In the case of a helical ICP, an induced magnetic field is distributed inside the cylindrical tube. Then, the plasma density can be determined by spatial distribution accordingly. Considering the domination of bulk ohmic heating in high-density plasma, we can assume that the plasma density is distributed on an axis only along the EM wave propagation direction. To estimate the EM wave propagation in the ICP plasma, we model the cosine distribution of plasma density to multi-layered isotropic media [27]. With the Drude model, the complex dielectric function of plasma is represented by

$$\hat{\varepsilon} = 1 - \frac{\omega_p^2}{\omega(\omega - j\nu_{eff})}, \quad (76)$$

Where  $\omega_p = \sqrt{4\pi ne/m_e}$  is the plasma frequency.  $n$  is the plasma density,  $e$  is the electric charge,  $m_e$  is the electron rest mass,  $\omega$  is the angular frequency of the electromagnetic wave, and  $\nu_{eff}$  is the effective collision frequency. When the plasma density follows a cosine distribution, it can be represented by

$$n(z) = n_0 f(z) = n_0 \cos(\pi z/l), \quad (77)$$

where  $n_0$  is a peak density in the cosine distribution,  $z$  is the axis of EM propagation direction, and  $l$  is length of plasma between the walls.

### 4.3.3 Axisymmetric two-dimensional multi-layer model for plasma sheath

Experimentally, the transmission converges to approximately -50 to -70 dB as opposed to total attenuation below the cut-off frequency in the multi-layered plasma model. To explain this, a plasma sheath is introduced near the edge of the plasma along the radial axis. With the assumption that the plasma-sheath density follow Boltzmann relation,  $n = n_0 \exp(-e\phi/k_b T_e)$  and the plasma potential  $\phi(r) \propto 1/(a - |r|)^2$  is defined with satisfying boundary condition ( $n(\pm a) = 0$ ). Where  $k_b$  is Boltzmann constant and  $T_e$  is the plasma temperature[28]–[30]. Therefore, cylindrical coordinate with its origin at the center of the plasma, the plasma density profile,  $n(r)$ , in the radial direction, can be expressed as

$$n(r) = n_0 f(r) = \begin{cases} n_0 \exp(K_1/(a - |r|)^2) & \text{if } (-a \leq r \leq s_0 - a) \text{ and } (a - s_0 \leq r \leq a) \\ n_0 & \text{if } (s_0 - a \leq r \leq a - s_0) \end{cases}, \quad (78)$$

where

$$s_0 \approx K_2 \times p^{-1/4} \times \sqrt{V_{rfm}}, \quad (79)$$

where  $p$  is gas pressure;  $s_0$  is the effective plasma sheath thickness;  $K_1, K_2$  is the correction factors; and  $V_{rfm}$  is the maximum RF voltage amplitude across the sheath [22], [31], [32]. Whereas the analysis of the plasma sheath is imprecise because of low SNR on the side lobes of the Gaussian beam, we can still roughly estimate the sheath size. Increasing the sheath thickness,  $s_0$ , affects the leakage field below the cut-off frequency region. Finally, we can derive the function of plasma density comprising a radially flat-topped distribution function and a longitudinally cosine distribution function. These two functions are represented by

$$n(r, z) = n_0 f(r) f(z). \quad (80)$$

For Gaussian-beam propagation in plasma, the transmittance in the 2D multi-layered plasma is not uniform in the radial position, as shown in Figure 4-6. Therefore, the average transmittance should be corrected with a weight function of the Gaussian distribution.

$$T' = \frac{\sum \alpha(r) \cdot T}{\sum \alpha(r)}, \quad (81)$$

where

$$\alpha(r) = \frac{e^{-(r/w(z))^2}}{\sum e^{-(r/w(z))^2}}, \quad (82)$$

where  $T'$  is the modified averaged transmittance by the weighted mean;  $\alpha(r)$  is a weight function of the Gaussian beam profile;  $r$  is a radial axis; and  $w(z)$  is the beam radius of the Gaussian beam [1]. In the theoretical model, we used optimized MATLAB codes for data comparison with experimental results, resulting in Eq. (83). Figure 4-7 shows excellent agreement between the experimental and fitted data.

$$\min \left( |T_{measurement} - T_{theory}|_{average} \right) < \text{Convergence error}. \quad (83)$$

The introduction of the plasma sheath is necessary to interpret the noise field in the cut-off region, as shown in the experimental data. Generally, Bessel-cosine function is defined as plasma density function for high pressure model[27]. However, Gaussian beam cannot be cut off completely in this condition. Although Gaussian beam can be cut off in central plasma, it can pass through the relatively lower density plasma on the outside of central plasma range ( $\omega > \omega_{pe}$ ). In a flat-topped model, the radial plasma density is higher than Bessel model's plasma density as shown in Figure 4-8(a). Therefore, the main lobe of Gaussian beam cannot penetrate to plasma except plasma-sheath regions. The Figure 4-7

show that transmittance of Bessel-cosine model is much higher than experimental results while the transmittance of flat-topped model is good agreement with experimental results.

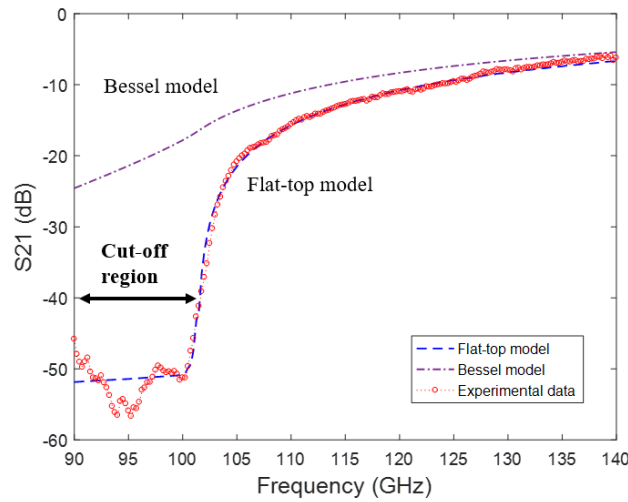


**Figure 4-7.** S21 (transmittance) result of experimental data compared to the axisymmetric 2D multi-layered models (flat-top and Bessel) data fitting (Ar gas, RF power: 1,000 W, pressure: 2 Torr)

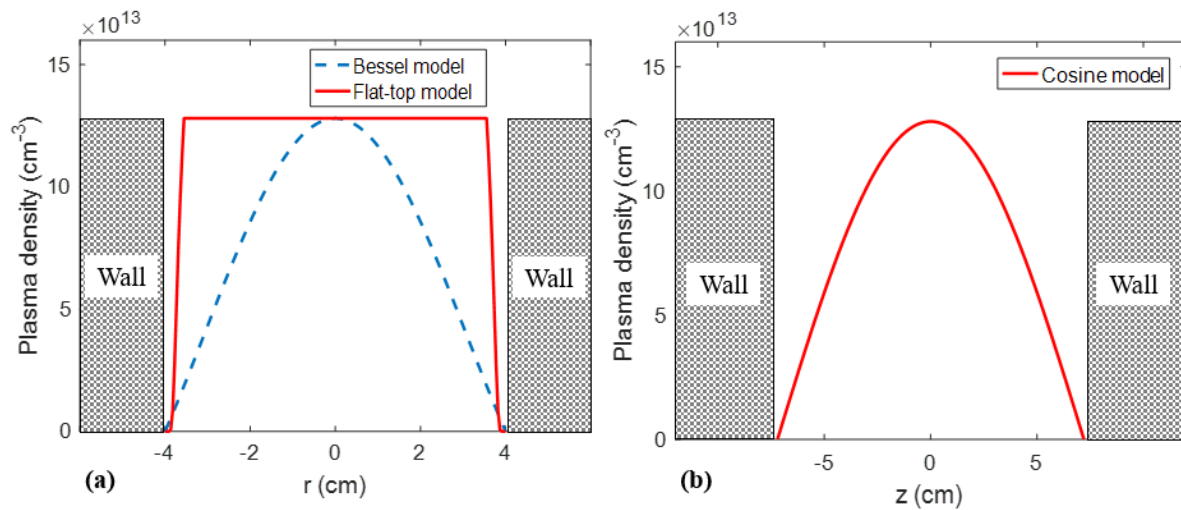


**Figure 4-8.** (a) The comparison of plasma density distributions between radial plasma models (r-axis, flat-top and Bessel models) (b) The axial plasma density distribution (z-axis, cosine model)

Based on the theoretical fitting results, we can extract the plasma densities and the effective collision frequencies when the RF power and gas pressure vary. Figure 4-10(a) shows that, as expected, an increase of RF power is proportional to the increase of plasma density in the Ar discharge. On the other hands, the increase of Ar gas pressure results in an increase of plasma density and a decrease of effective collision frequency. The former behavior follows extant results of ICP plasma experiments [33], [34] and the latter behavior follows G. G. Lister's report[35] within Maxwellian distribution.

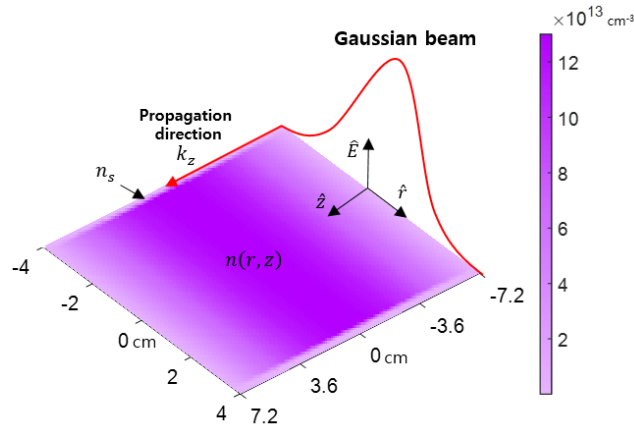


**Figure 4-9.** Axisymmetric 2D multi-layered model with Gaussian-beam propagation

In low electron temperature ( $T_e \leq 2$ ) and high-pressure condition ( $p \geq 1$  torr), the  $v_{eff}/p$  is under 1. It is well agreement with Fig. 4-10(b). In addition, the RF power is independent from the effective collision frequency, whereas an increase of gas pressure is inversely proportional to the increase of the effective collision frequency, as observed in Fig. 4-10(b) [35], [36].

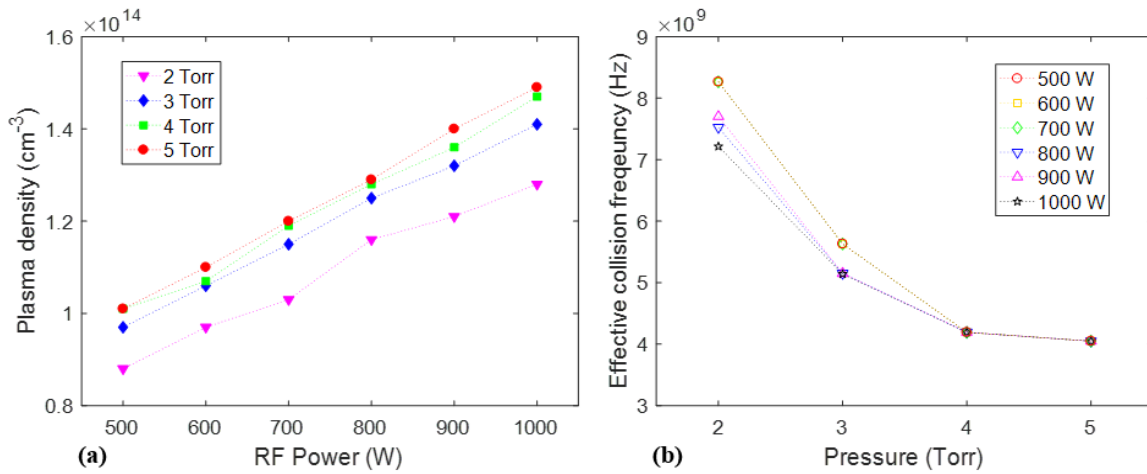


**Figure 4-10.** (a) Graph of plasma densities vs. RF power via the fitting model (Std. Dev. =  $\pm 0.01 \times 10^{14}$  cm<sup>-3</sup>). (b) Graph of effective collision frequencies vs. pressure via the fitting model (Std. Dev. =  $\pm 4.18 \times 10^8$  Hz)

Using plasma-sheath analysis, we can estimate the effective plasma-sheath thickness by assuming that the plasma density in the sheath is defined by Eq. (78). The effective plasma-sheath thickness is decrease when the gas pressure is increase and RF power is increase, as predicted. We exclude a few of fitting data under conditions of 500W RF (in 2 – 5 Torr) and 600 ~ 700W (at 2 Torr) in Figure 4-11. The reason is that the step lines caused by the cut-off frequency are out-of-range in the frequency

domain (90–140 GHz). Considering the Figure 4-11, we can estimate that the effective plasma-sheath thickness is decrease with an increasing plasma density.

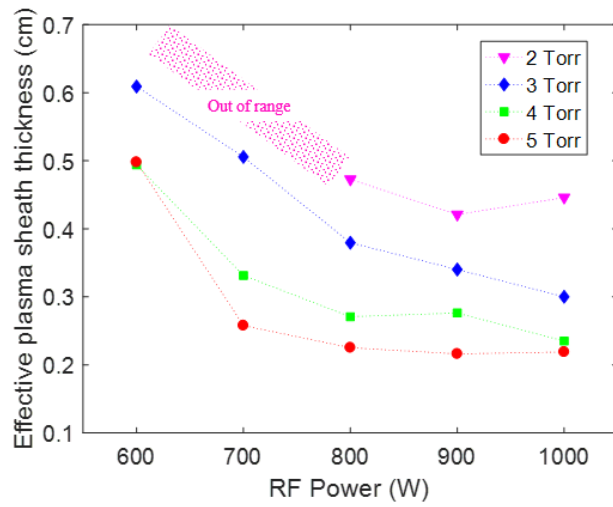


**Figure 4-11.** Estimated effective plasma-sheath thickness by theoretical modeling



## 4.4 Fast control of high-power millimeter pulse in pulsed plasma

### 4.4.1 Gyrotron: high-power millimeter wave source

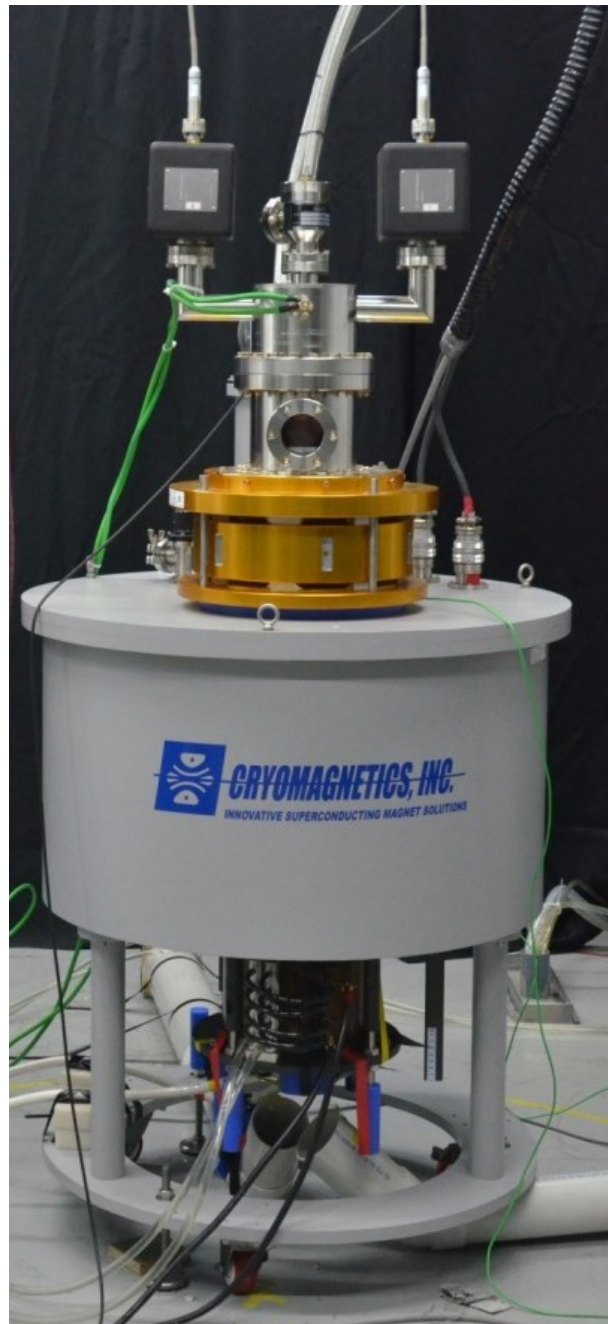


**Figure 4-12.** UNIST W-band gyrotron

For fast control test of high-power millimeter-wave using pulsed plasma, the kW gyrotron made by UNIST is used as high-power millimeter-wave source. The measured frequency is 95.15 ~ 95.18 GHz (Band width: 30 MHz), the pulse length is 20us and output power is approximately 20 kW.

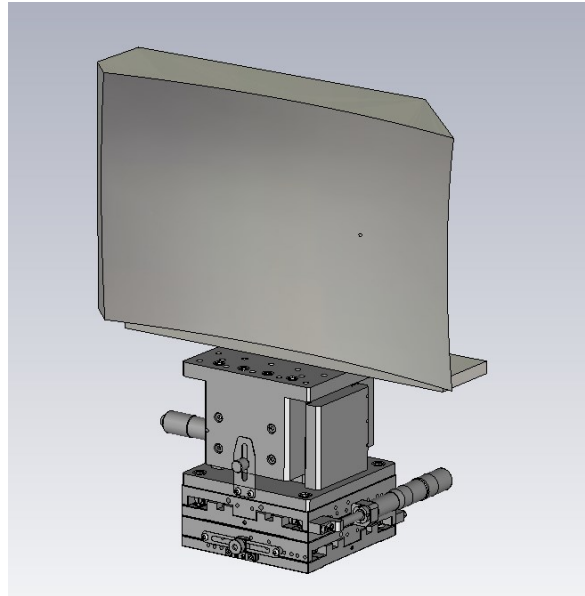


**Figure 4-13.** Focusing mirror for gaussian beam injection

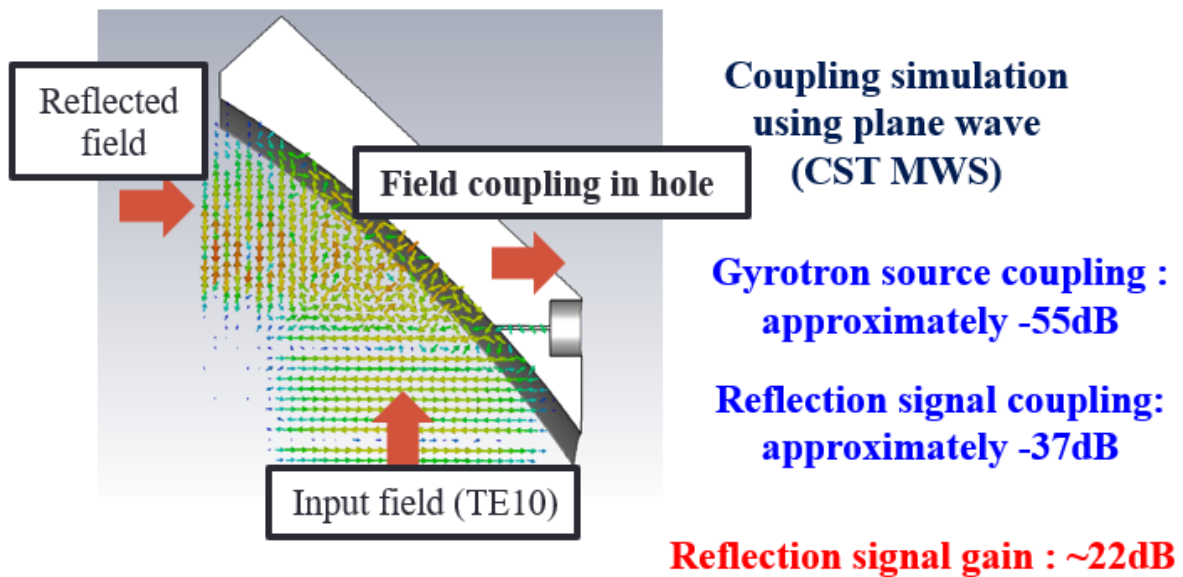


**Figure 4-14.** CST MWS simulation of reflection gain measurement in focusing mirror

#### 4.4.2 Focusing mirror

The radiated EM wave from gyrotron should be focused to plasma chamber without loss in free space. Therefore, quasi-optical focusing mirror is design based spherical mirror structure as shown in Figure 4-13. The radius of curvatures in vertical and horizontal axis is different for optimize Gaussian beam. This quasi-optical focusing mirror is usually called ‘matching optics unit (MOU)’ in ECH & CD transmission lines. Additionally, we drill a hole on mirror for reflection measurement. To increase reflection gain, we minimize input field coupling (-55 dB) in CST simulation as shown in Figure 4-14. The MOU is demonstrated by Surf3D code with the EM field results from quasi-optical mode converter

in gyrotron. The Gaussian beam coming from gyrotron is not perfect gaussian beam so beam waist of vertical and horizontal is different. Therefore, we design mirror having horizontal the radius of curvature is 80 cm and vertical the radius of curvature is 40 cm. the reflected beam is focused to plasma chamber position with 1 cm of beam waist as described in Figure 4-15.

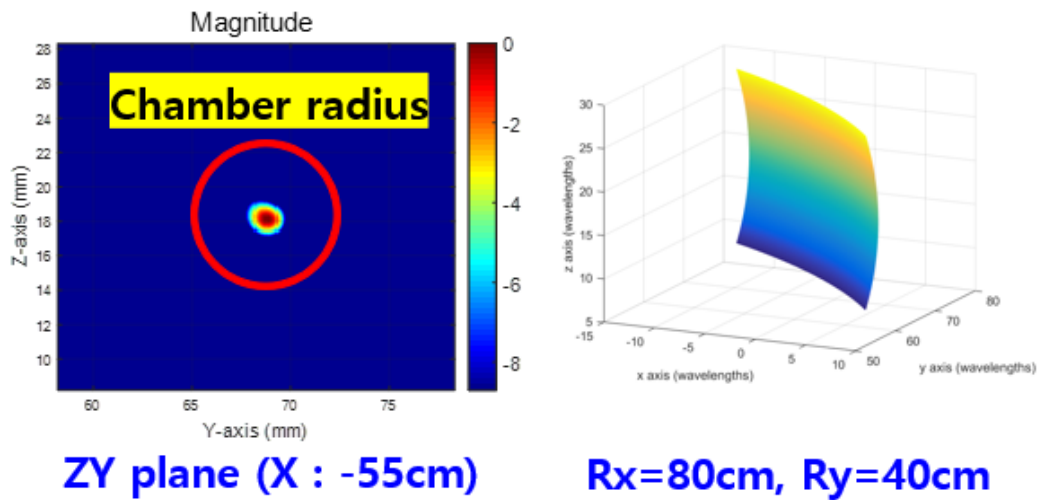


**Figure 4-15.** Focused gaussian beam at plasma chamber with designed focusing mirror mesh

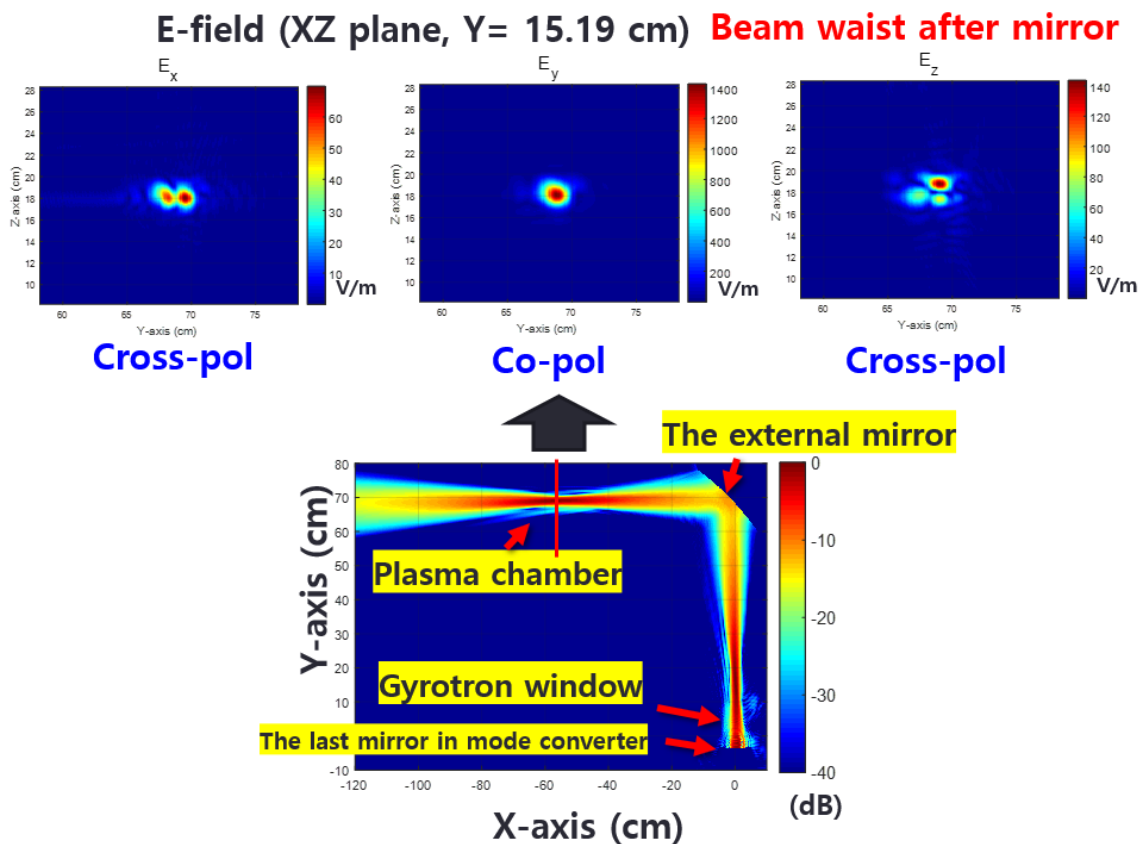


**Figure 4-16.** The experimental setup of high-power millimeter-wave absorption in pulsed plasma Focused gaussian beam at plasma chamber with designed focusing mirror mesh

In Figure 4-16, co-polarization of field is propagated along with horizontal direction. It is same direction before EM field is reflected to mirror. In addition, The Gaussian beam can be propagated to plasma chamber without strong diffraction and reflection. The MOU is fabricated by 5-axis CNC machine using aluminum in UNIST. In MOU, the small hole is drilled for reflection measurement along with injection direction.

#### 4.4.3 Experimental setup

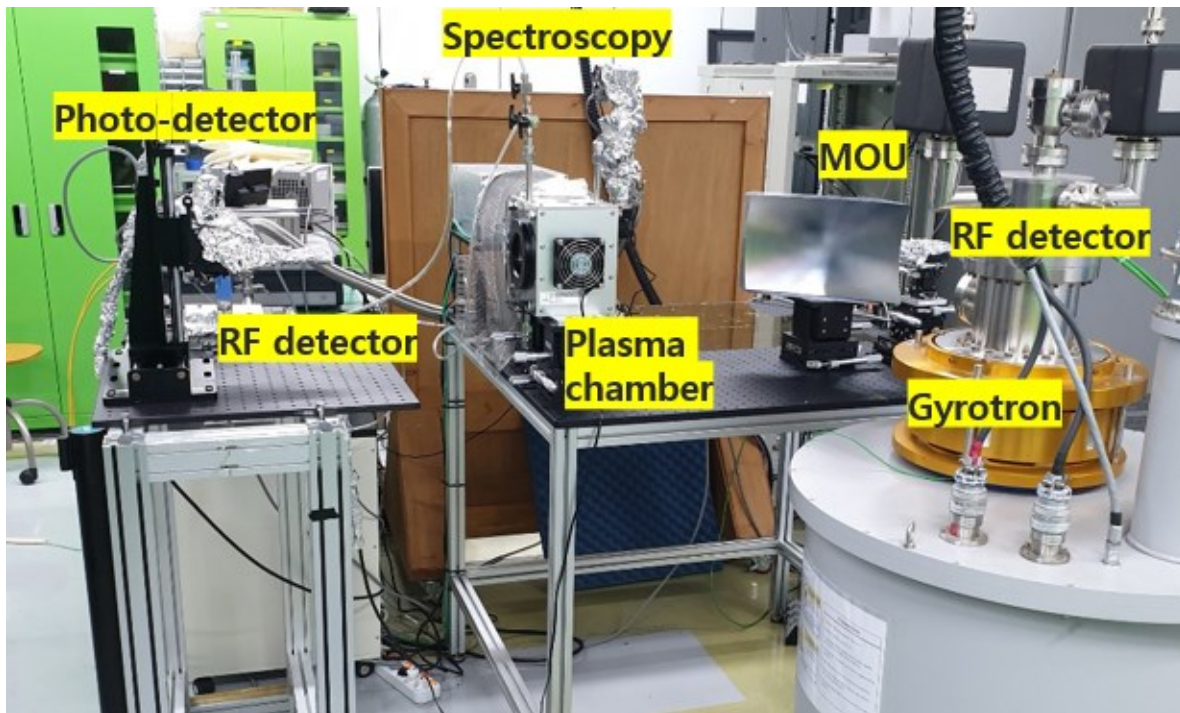


**Figure 4-17.** The experimental setup of high-power millimeter-wave absorption in pulsed plasma

The system consists of gyrotron part and plasma part. In Figure 4-14, Gyrotron is settled in superconductor magnet. The MOU mirror should be aligned for transfer the Gaussian beam to plasma as shown in Figure 4-18. Figure 4-19 shows initial Gaussian beam is tilted in horizontal direction. The millimeter-wave Schottky diode detectors are aligned to 1 m distance from MOU and back of MOU hole. The Schottky diode detectors measure the transmittance and the reflectance of high-power millimeter-wave after plasma absorption effect. In other hands, the photodetector is installed on the plasma chamber and optical emission spectroscopy is also installed for analysis of optical emission spectrum coming from plasma discharge. In this configuration, we conduct experiment to identify absorption of high-power millimeter-wave in plasma. The inductive RF plasma is discharged in 3 Torr of pressure and 1000 W of RF power.

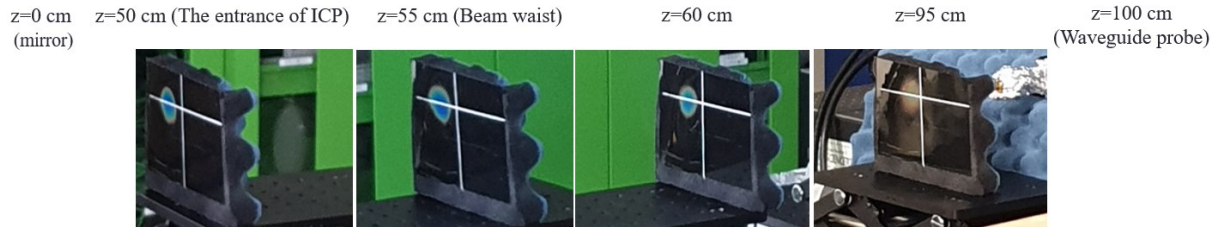


**Figure 4-18.** Gyrotron alignment using field tracing on liquid crystal paper

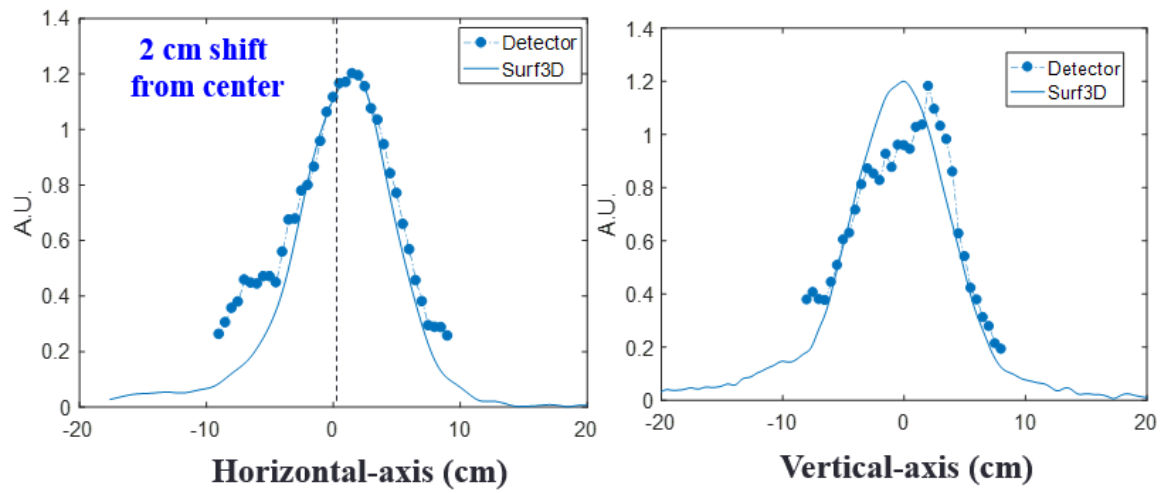


**Figure 4-19.** Gyrotron beam 1D scan results at focusing mirror position

#### 4.4.4 Absorption of high-power millimeter wave in steady-state plasma

When plasma is generated in steady state, a high-power millimeter-wave is launched to plasma. In 3 Torr pressure, an estimated effective collision frequency is around 5.15 GHz. In this condition, absorption can be highest when plasma density is smaller than plasma cut-off density. To analyze experimental results, we conduct COMSOL multi-physics simulations using wave optics module. The plasma is simply defined as a complex media by pervious work. Based on existing plasma density information's, we can get transmittance, reflectance and absorption of Gaussian beam in plasma. We used parametric sweep for observe change of absorption ratio when plasma density is increase. We can find that absorption rate is highest at  $10.8 \times 10^{14} \text{ cm}^{-3}$ . In the other hands, we can find transmittance and reflectance of high-power millimeter-wave using Schottky diode detector in experiment. In Figure 4-22(a), transmittance of millimeter-wave is gradually decrease when RF power is increase. Meanwhile, a photodetector signal is measured by response of plasma absorption. The optical emission signal is abruptly increase with the ratio of high-power millimeter-wave signal as described in Figure 4-22(c). These results are well agreement with COMSOL simulation results. We can estimate that absorption of high-power millimeter-wave make plasma density increase.

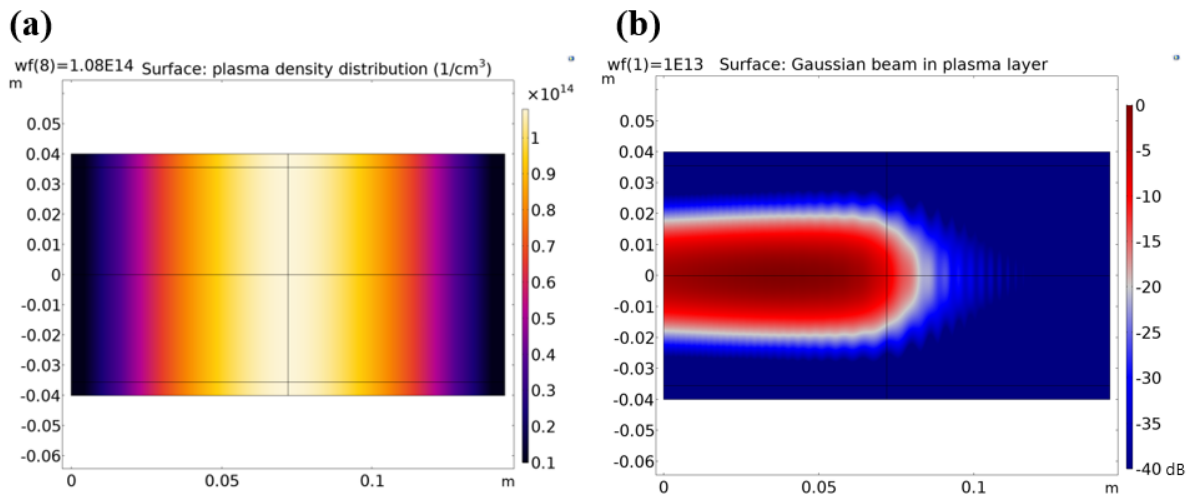


**Figure 4-20.** COMSOL Multiphysics simulation (a) Plasma density distribution (b) Gaussian beam absorption in plasma (Initial peak plasma density:  $1.08 \times 10^{14} \text{ cm}^{-3}$ , Effective collision frequency: 5.15GHz)

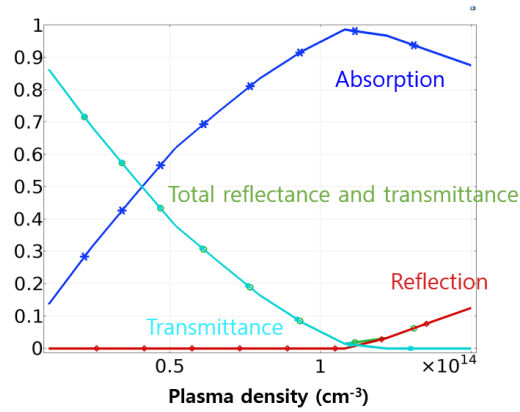


**Figure 4-21.** Transmittance, reflectance and absorption of Gaussian beam in plasma (COMSOL Multiphysics)

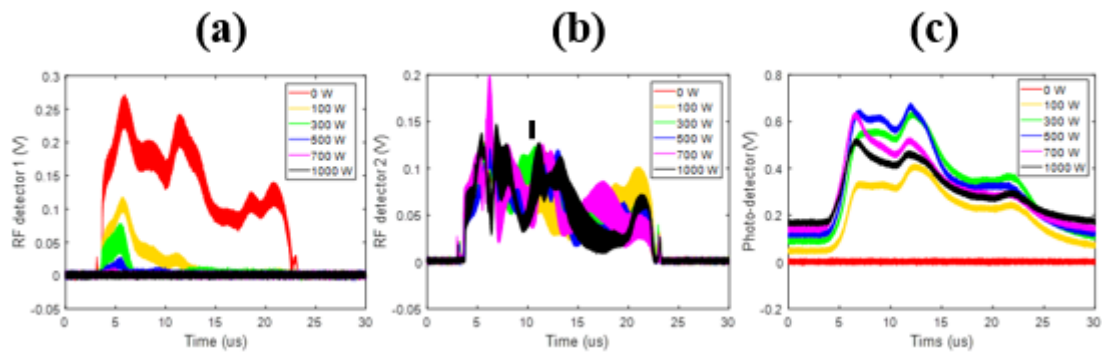


**Figure 4-22** (a) Transmittance of gyrotron pulse with RF power dependence (b) Reflectance of gyrotron pulse with RF power dependence (c) Photodetector signal with RF power dependence



#### 4.4.5 High-power millimeter-wave in pulsed plasma for plasma switching system.

Based on results of high-power millimeter-wave in steady-state plasma, we tried to extend high-power millimeter-wave in pulsed plasma for fast switching application of high-power millimeter-wave using plasma switching system. However, plasma parameter (plasma density and effective collision frequency) of pulsed plasma is different with steady state plasma. We should check low power millimeter wave interaction in pulsed plasma for understand physical effects before high-power millimeter-wave test. Figure 4-23 shows low-power millimeter-wave test using VNA source and Schottky diode detector in QO systems. Source is a continues wave (CW) so it is convenient to observe plasma state.

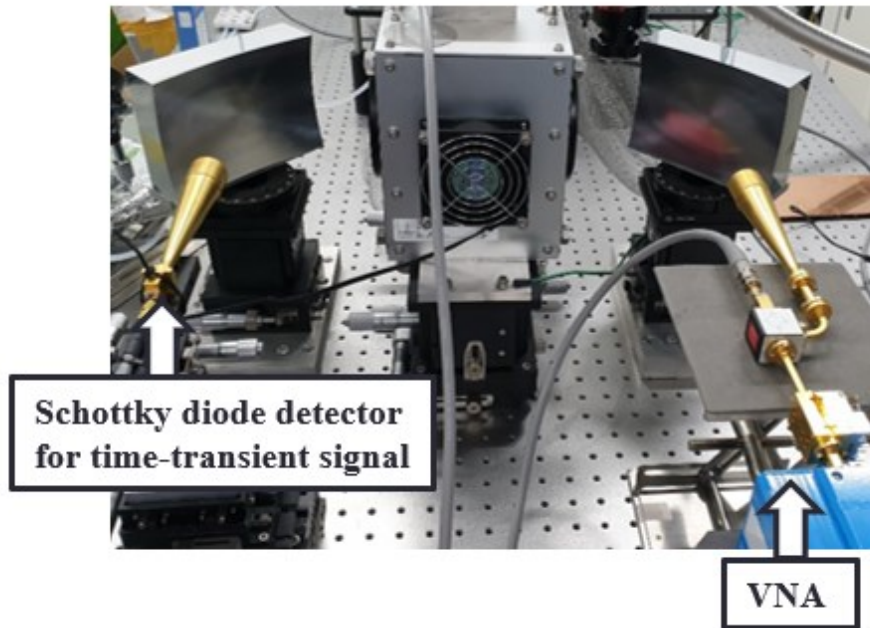


**Figure 4-23.** Experimental setup of low-power millimeter-wave switching test

In several times of experiments, we found optimized plasma condition varying RF pulsing condition in RF generator. Argon gas was injected in plasma chamber with 2 Torr pressure and 1 kW of RF power is supplied to plasma. The estimated plasma density is  $1.28 \times 10^{14} \text{ cm}^{-3}$  and effective collision frequency is 6.96 GHz. RF power was driven in 0.5 kHz with 30 % duty cycle. The Figure 4-24 shows that experimental results of low power millimeter-wave in pulsed plasma. In plasma on state, photo-detector signal immediately jumps up and slowly decay up to steady state on 0.2 V. In other hands, millimeter-wave signal from Schottky diode detector not immediately goes down because of plasma generation time and plasma density fluctuation coming from impedance matching instability. After few hundreds

of microseconds, the signal maintains in low transmission (< 50%) even if RF pulse is turn off. We can deduce plasma rise time and decay time cannot follow RF switching time. The delay time is almost 300 us. In plasma off state, photo-detector signal is slowly converged to 0 V and millimeter-wave signal maintains in high transmission level (> 70%). However, loss of millimeter-wave is still left because plasma is not totally turn off. Finally, we can define millimeter-wave on time is 1200 us and millimeter-wave off time is 800 us in 1 cycle.

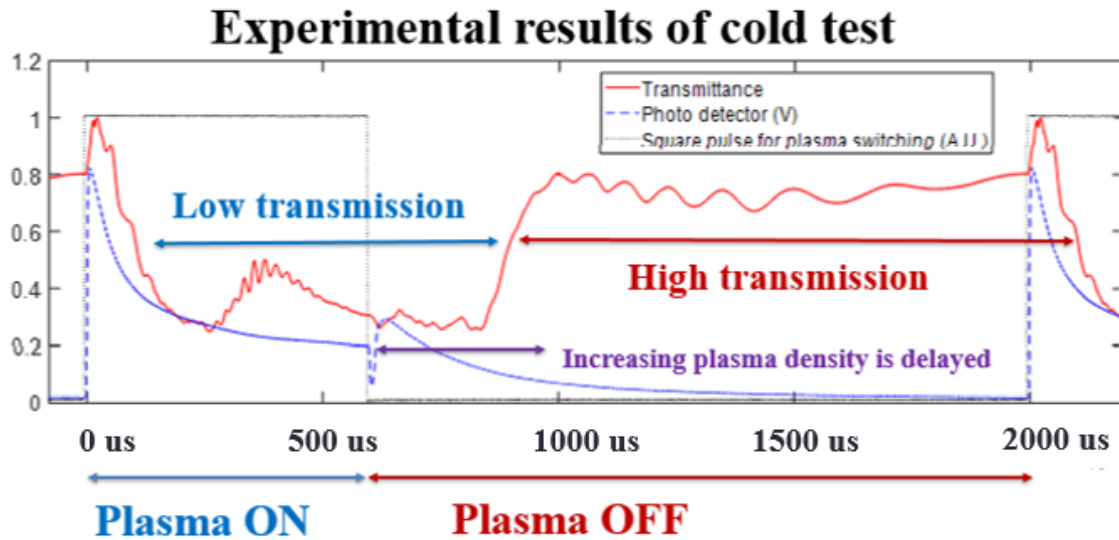


**Figure 4-24.** Experimental results of low-power millimeter-wave switching test

To compare with high-power test experiments, we display table about difference of low power and high-power conditions in Figure 4-25. In case of VNA source, it cannot invasive pulsed plasma because power level is few of mW. In case of gyrotron pulse, absorbed millimeter-wave energy invasive to pulsed plasma.

	VNA continues-wave (CW)	Gyrotron pulse
<b>Pulse length</b>	Continuous wave (CW)	20 us
<b>Power</b>	13 dBm	20 kW
<b>Interaction with plasma</b>	Non-invasive	Invasive

**Figure 4-25.** Comparison of lower-power test and high-power test

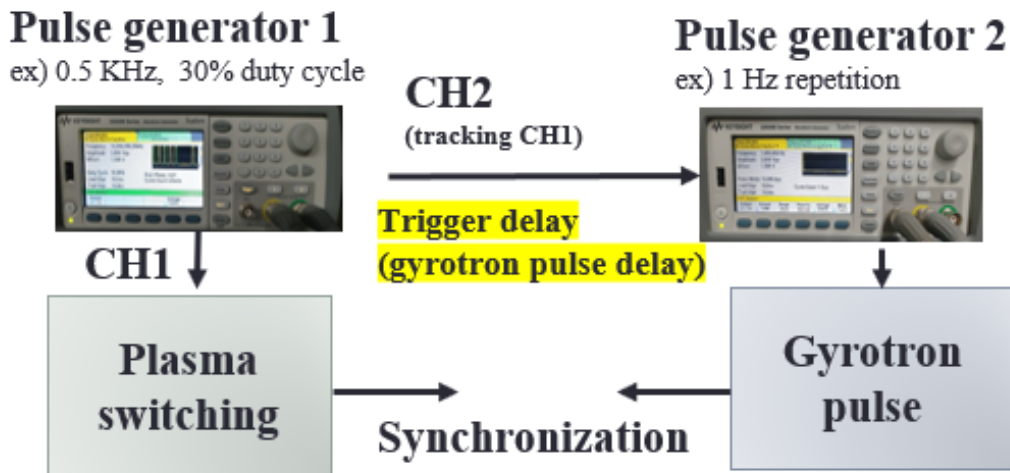


**Figure 4-26.** Selective injection of gyrotron pulse in pulsed plasma using pulse synchronization

The plasma switching system is designed for fast control of high-power millimeter-wave. The pulsed plasma can be generated using function of RF pulsing in RF generator (13.56 MHz, 1000 W). However, switching period have a limitation because of plasma decay and rise time in previous low power test. When switching period is 0.5 kHz and duty cycle is 30%, 20 us gyrotron pulse is launched in pulsed plasma. Gyrotron pulse is very shorter than plasma ‘ON’ time. Therefore, Gyrotron pulse is selectively launched to plasma using delayed synchronization technique in the Figure 4-26. This technique uses pulse generators. The trigger signal form first pulse generator for plasma switching can transfer the same trigger signal to second pulse generator for Gyrotron pulse. Then, we can make delay time between two of trigger signal. In this condition, the experimental results were collected in Figure 4-27. The optical emission signal is jumped when gyrotron pulse is absorbed in plasma. Although the plasma is ‘OFF’ state, plasma still strongly absorb to gyrotron pulse before initial section of plasma ‘OFF’ (Plasma OFF time is under 25% of total plasma OFF time). However, Gyrotron pulse is pass through plasma after half section of plasma ‘OFF’ (Plasma OFF time is over 50% of total plasma OFF time).

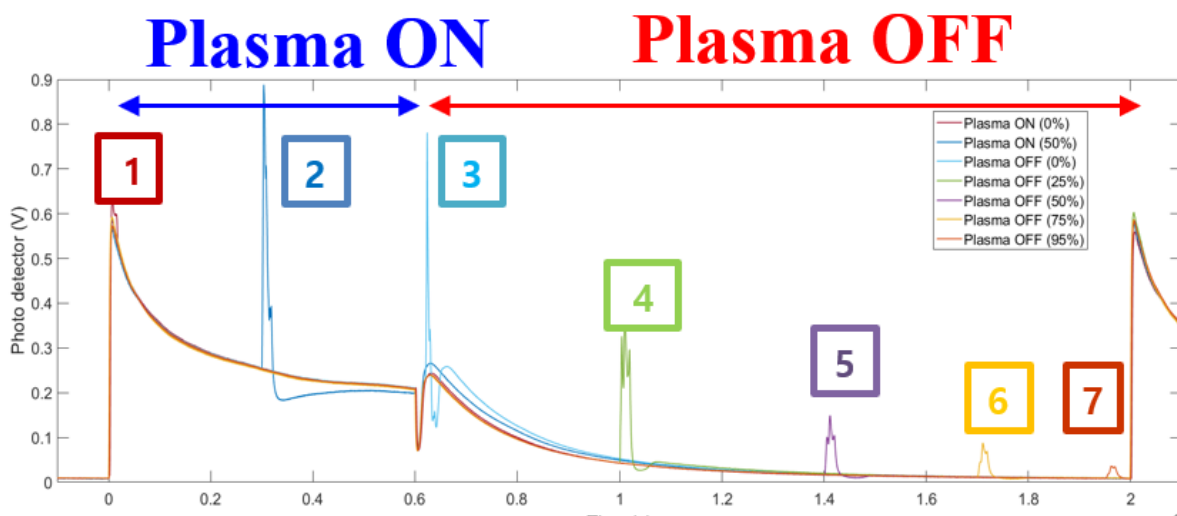


**Figure 4-27.** Selective injections of Gaussian beam in pulsed plasma.

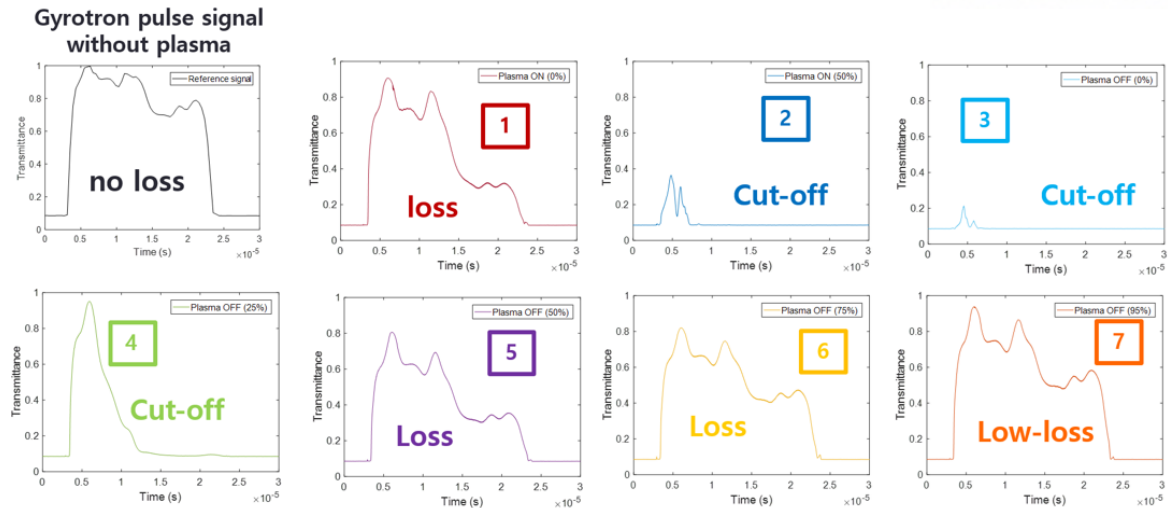


**Figure 4-28.** The transmittances of Gaussian beam in pulsed plasma at each selective injection.

Furthermore, Gyrotron pulse cannot absorb to plasma in initial section of Plasma ‘ON’. From this results, Gyrotron pulse is only strongly absorbed a limited plasma period in low transmission region as shown in Figure 4-24 (2, 3 and 4 section in Figure 4-27 and Figure 4-28). Specially, we can find rise time of plasma density by Gyrotron pulse in Figure 4-28 (section 4). Therefore, an absorbed gyrotron pulse can increase and decrease plasma density immediately. This rise time and decay time is very shorter than the time in RF discharged plasma. The relationship of RF frequency and plasma decay time should be studied additionally. Furthermore, this effect can disturb maintaining plasma ‘OFF’ state when absorption is maintained when plasma is ‘OFF’. If we assume that CW of high-power millimeter-wave, absorbed millimeter-wave will increase plasma density and maintain cut-off plasma density on section 4. Understanding plasma physics in pulsed plasma with high-power millimeter-wave absorption is very challengeable because the plasma density and effective collision frequency is periodically change but also high-power millimeter-wave absorption have effects of change of plasma parameter. Novel diagnostics system is needed so that these effects should be distinguishable.

# Chapter 5

## Conclusion

In conclusion, we developed a quasi-optical transmission system for probing plasma density and carrier density in semi-conductor. A high-efficiency quasi-optical transmission line with a transmittance of more than 95% was experimentally achieved. Not only the basic properties of a Si sample but also the carrier lifetime for a single decay function were measured by using the theoretical fitting model with 2D mapping. The proposed QO-PCD method can be used to measure the carrier lifetime at a high injection level ( $\sigma_0 \ll \Delta\sigma$ ). In spite of various advantages, the QO-PCD system has potential limitations related to the thickness and the conductivity of the semiconductor, similarly to the u-PCD method. Therefore, the QO-PCD should apply the sub-millimeter regime to increase the response of decay time. In addition, the system can be change to a reflectivity measurement setup to measure doped silicon wafers with doping densities of  $10^{15}$ – $10^{17}$   $\text{cm}^{-3}$ .

In plasma part, the diagnosis of high-density plasmas ( $10^{13}$ – $10^{14}$   $\text{cm}^{-3}$ ) was successfully performed using a newly developed non-invasive quasi-optical transmission system in F-band millimeter waves. We have thus proposed a theoretical fitting model with axisymmetric 2D multi-layered plasma density. In the cylindrical high-density plasma of the helical ICP chamber, we estimated that the plasma density profile along the longitudinal z-axis followed a cosine distribution, based on our results. Along the radial axis, the plasma density distribution was flat-topped model which central plasma is almost constant with plasma sheath layer near the edge of the chamber wall. Whereas the theoretical model showed very good agreement with the experimental results, the theoretical model still had limitations, owing to the uncertainties of measurement and physical conditions. First, the analysis of the plasma sheath was insufficient for estimating sheath thickness and spatial density profile because it was measured in a cut-off frequency region of low SNR (-50 to -70 dB). Second, the wavelength depended on the quasi-optical beam size and the plasma size, which may have limited the localized measurement under low-plasma density. Nonetheless, the sensitivity of this method was higher than that of the other methods, based on free-space RF measurement techniques. Furthermore, applying the technique for localized measurements (a few  $\text{mm}^2$ ) is promising for higher-density plasma ( $10^{14}$ – $10^{17}$   $\text{cm}^{-3}$ ) regions when using THz waves for various applications. In a future study, the theoretical model will be modified

for advanced plasma physical parameters and fusion plasma applications. We also may develop an application for the proposed system to measure time-dependent plasma density.

In high-power millimeter-wave section, we conducted experiments of high-power millimeter-wave absorption in steady-state plasma and pulsed plasma. Quasi-optical focusing mirror is designed and fabricated for focus to plasma chamber with low loss. In experiment, high-power millimeter-wave can be absorbed in steady-state plasma without high reflection. In other hand, pulsed plasma can pass high-power millimeter-wave in plasma 'OFF' time. However, absorption of high-power millimeter-wave in plasma can increase plasma density. This effect will disturb fast control of high-power millimeter-wave. The different gas and other plasma condition should be explored.

# References

- [1] P. F. Goldsmith, I. of Electrical, E. Engineers, M. Theory, and T. Society, *Quasioptical systems: Gaussian beam quasioptical propagation and applications*. IEEE press New York, 1998.
- [2] E. Håkansson, A. Amiet, and A. Kaynak, “Dielectric characterization of conducting textiles using free space transmission measurements: Accuracy and methods for improvement,” *Synth. Met.*, vol. 157, no. 24, pp. 1054–1063, 2007.
- [3] Y. P. Hong, M. J. Salter, and D. J. Lee, “Broadband measurement of high permittivity at millimetre-wave frequencies,” *Electronics Letters*, vol. 52, no. 9. pp. 725–727, 2016.
- [4] D. K. Ghodgaonkar, V. V. Varadan, and V. K. Varadan, “Free-Space Measurement of Complex Permittivity and Complex Permeability of Magnetic Materials at Microwave Frequencies,” *IEEE Trans. Instrum. Meas.*, vol. 39, no. 2, pp. 387–394, 1990.
- [5] M. Wang *et al.*, “Propagation matrix method study on THz waves propagation in a dusty plasma sheath,” *IEEE Trans. Antennas Propag.*, vol. 64, no. 1, pp. 286–290, 2016.
- [6] J. Schmidt, “Measuremnt of differential and Actual Recombination parameters on Crystalline Si wafers,” *IEEE Trans. Electron Devices*, vol. 46, pp. 2018–2025, 1999.
- [7] M. Kunst and G. Beck, “The study of charge carrier kinetics in semiconductors by microwave conductivity measurements,” *J. Appl. Phys.*, vol. 60, no. 10, p. 3558, 1986.
- [8] R. K. Ahrenkiel and S. W. Johnston, “Interaction of microwaves with photoelectrons in semiconductors,” *J. Vac. Sci. Technol. B Microelectron. Nanom. Struct.*, vol. 26, no. 4, p. 1508, 2008.
- [9] K. Lauer, A. Laades, H. Übensee, H. Metzner, and A. Lawerenz, “Detailed analysis of the microwave-detected photoconductance decay in crystalline silicon,” *J. Appl. Phys.*, vol. 104, no. 10, p. 104503, 2008.
- [10] M. S. Choe, A. Sawant, K. S. Lee, N. E. Yu, and E. M. Choi, “Measuring the carrier lifetime by using a quasi-optical millimeter- and THz-wave system,” *Appl. Phys. Lett.*, vol. 110, no. 7, pp. 1–5, 2017.
- [11] T. Vogel, G. Dodel, E. Holzhauser, H. Salzmann, and A. Theurer, “High-speed switching of far-infrared radiation by photoionization in a semiconductor,” *Appl Opt*, vol. 31, no. 3, pp. 329–337, 1992.
- [12] S. M. Sze and K. K. Ng, *Physics of semiconductor devices*. John wiley & sons, 2006.
- [13] M. Born and E. Wolf, “Principles of optics,” *Pergamon, New York*, vol. 19891, pp. 747–754,

- 1980.
- [14] J. A. Murphy, “Distortion of a simple Gaussian beam on reflection from off-axis ellipsoidal mirrors,” *Int. J. Infrared Millimeter Waves*, vol. 8, no. 9, pp. 1165–1187, 1987.
  - [15] Y. Minami, K. Horiuchi, K. Masuda, J. Takeda, and I. Katayama, “Terahertz dielectric response of photoexcited carriers in Si revealed via single-shot optical-pump and terahertz-probe spectroscopy,” *Appl. Phys. Lett.*, vol. 107, no. 17, p. 171104, 2015.
  - [16] B. Donovan and N. H. March, “High Frequency Conductivity in Semiconductors,” *Proc. Phys. Soc. Sect. B*, vol. 69, no. 5, p. 528, 1956.
  - [17] R. J. Kumar *et al.*, “Microwave photoconductivity decay characterization of high-purity 4H-SiC substrates,” *J. Appl. Phys.*, vol. 102, no. 1, p. 13704, 2007.
  - [18] J. Kang, J. Kim, C. Cho, and D. Kim, “자유공간 물질상수 측정법을 이용한 W-Band 유전율 측정,” *Korean Inst. Electromagn. Eng. Sci*, vol. 24, no. 3, pp. 253–258, 2013.
  - [19] J. Baker-Jarvis, M. D. Janezic, J. H. Grosvenor, and R. G. Geyer, “NIST Technical Note 1355-R,” *NIST, Boulder USA*, p. 20, 1993.
  - [20] M. A. Lieberman and A. J. Lichtenberg, *10\_Particle and Energy Balance. .*
  - [21] K. Niazi, A. J. Lichtenberg, M. A. Lieberman, and D. L. Flamm, “Operation of a helical resonator plasma source,” *Plasma Sources Sci. Technol.*, vol. 3, no. 4, pp. 482–495, 1994.
  - [22] L. M.A., L. A.J., and F. D.L., *Theory of a helical resonator plasma source*. 1990.
  - [23] J. Neilson, “Surf3d and LOT : computer codes for design and analysis of high-performance QO launchers in gyrotrons,” *Infrared Millim. Waves Conf. Dig. 2004 Jt. 29th Int. Conf. 2004 12th Int. Conf. Terahertz Electron. 2004*, pp. 667–668, 2004.
  - [24] J. Neilson and R. Bunger, “Surface integral equation analysis of quasi-optical launchers using the fast multipole method,” *Conf. Dig. - 27th Int. Conf. Infrared Millim. Waves, IRMMW 2002*, vol. 30, no. 3, pp. 119–120, 2002.
  - [25] U. Manual, “Surf3d,” 2018.
  - [26] V. L. Ginzburg, W. L. Sadowski, D. M. Gallik, and S. C. Brown, *Propagation of Electromagnetic Waves in Plasma*, vol. 15, no. 10. 1962.
  - [27] M. A. Lieberman and A. J. Lichtenberg, *Principles of plasma discharges and materials processing*, vol. 2. Wiley Online Library, 2005.
  - [28] V. A. Godyak and N. Sternberg, “Smooth plasma-sheath transition in a hydrodynamic model,” *IEEE Trans. plasma Sci.*, vol. 18, no. 1, pp. 159–168, 1990.
  - [29] T. E. Sheridan and J. Goree, “Collisional plasma sheath model,” *Phys. Fluids B*, vol. 3, no. 10, pp. 2796–2804, 1991.
  - [30] S. V. Berezhnoj, C. B. Shin, U. Buddemeier, and I. Kaganovich, “Charged species profiles in oxygen plasma,” *Appl. Phys. Lett.*, vol. 77, no. 6, pp. 800–802, 2000.



- [31] I. Transactions, O. N. Plasma, and S. Vol, “Dynamics of a collisional, capacitive RF sheath - Plasma Science, IEEE Transactions on,” vol. 17, no. 2, pp. 338–341, 1989.
- [32] G. R. Misium, L. A.J., and L. M.A., “Macroscopic modeling of radio-frequency plasma discharges,” *J. Vac. Sci. Technol. A*, vol. 7, no. 3, pp. 1007–1013, 1989.
- [33] D. Jang, H. S. Uhm, D. Jang, M. S. Hur, and H. Suk, “Electron density characterization of inductively-coupled argon plasmas by the terahertz time-domain spectroscopy,” *Plasma Sources Sci. Technol.*, vol. 25, no. 6, p. 65008, 2016.
- [34] S. M. Meier, T. V. Tsankov, D. Luggenhölscher, and U. Czarnetzki, “Measurement of plasma densities by dual frequency multichannel boxcar THz time domain spectroscopy,” *J. Phys. D. Appl. Phys.*, vol. 50, no. 24, 2017.
- [35] G. G. Lister, Y. M. Li, and V. A. Godyak, “Electrical conductivity in high-frequency plasmas,” *J. Appl. Phys.*, vol. 79, no. 12, pp. 8993–8997, 1996.
- [36] K. H. You *et al.*, “Measurement and analysis of electron-neutral collision frequency in the calibrated cutoff probe,” *Phys. Plasmas*, vol. 23, no. 3, 2016.

## Acknowledgement

학위과정 동안 다양한 사람들과 선후배들 그리고 지도교수님을 만나면서 인생의 밑거름을 다지는 기간이 되었다고 생각합니다. 순수하게 연구가 좋아서 시작하였지만 많은 경험과 시련을 겪으면서 저의 부족한 점을 다시 한번 깨닫고 어떻게 인생을 살아가야 될지 배우는 기회가 되었습니다. 선배 연구자로서 인생의 선배로서 많은 조언을 해준 최은미 교수님께 다시 한번 감사하다는 말 전하고 싶습니다. 그리고 연구실 생활을 함께 해온 동료들에게도 정말 고맙다는 말 전하고 싶습니다. 동료들의 도움이 없었다면 절대 여기까지 도달하지 못하였을 것입니다. 많이 힘들고 지칠 때도 묵묵히 기다려 주고 응원해준 부모님과 누나에게도 진심으로 감사의 말 드립니다.

앞으로도 독립적인 연구자로서 물리학자로서 초심을 잃지 않고 사랑하는 가족과 친구들의 소중함을 잃지 않고 잘 헤쳐 나갈 수 있도록 정진하겠습니다.

06/05/2019

최문석